1   Phase Transitions of Multi-component Fuel Droplets under Sub- and Supercritical Conditions

2   Yifei Gong[a], Guowei Xiao[a], Xiao Ma[a, *], Kai Hong Luo[b], Shijin Shuai[a], Hongming Xu[a,c]

3   [a] State Key Laboratory of Automotive Safety and Energy, Tsinghua University, Beijing 100084, China

4   [b] Department of Mechanical Engineering, University College London, Torrington Place, London WC1E

5   7JE, UK

6   [c] Department of Mechanical Engineering, University of Birmingham, Birmingham B15 2TT, UK

7

8   Abstract: For a multi-component hydrocarbon mixture under supercritical conditions, the mechanism and

9   criterion for the transition of the dominant mixing mode from evaporation to diffusion are not well

10   established. In this paper, phase transition processes of three-component hydrocarbon fuel (5.3 wt%

11   isooctane, 25.8 wt% n-dodecane and 68.9 wt% n-hexadecane) droplets in sub- and supercritical nitrogen

12   environments were studied using molecular dynamics, in comparison with those of single-component n-

13   hexadecane droplets. The initial diameters of the droplets were 25.5 nm (three-component) and 26.5 nm

14   (single-component), respectively. Based on the quantitative Voronoi tessellation, a new criterion, which

15   was a combination of two dimensionless critical values of $H_c = 0.85$ and $W_c = 0.35$, was proposed to

16   determine the transition of the dominant mixing mode from evaporation to diffusion during fuel-ambient

17   gas mixing. The droplet evaporation lifetime, initial heat-up time and evaporation rate constant were

18   analyzed for all simulation cases. Effects of ambient temperature and ambient pressure on the dominant

19   mixing mode transition were discussed. Results indicated that when the ambient pressure ranged from 2

20   MPa to 10 MPa and the ambient temperature ranged from 750 K to 1200 K, the density difference between

21   the vapor phase and the liquid phase decreased gradually with increasing ambient pressure or decreasing

22   ambient temperature. In the meantime, the dominant mixing mode gradually transitioned from evaporation

23   to diffusion. A new parameter, the vapor-liquid equal probability time $t_{pv\,=\,pl}$, was proposed to evaluate

24   the phase transition speed of hydrocarbon fuels. Increasing the ambient pressure did not necessarily

25   promote the occurrence of phase transition, while increasing ambient temperature accelerated the phase

26   transition monotonically. The dominant mixing mode maps on the P-T diagram for evaporation systems

27   of pure n-hexadecane droplets and three-component fuel droplets were presented. The addition of light

28   components increased the minimum pressure of the mixing zone dominated by diffusion. A major finding

29   was that under a certain ambient pressure, the ambient temperature where the fuel could undergo

30   supercritical transition in ambient gas had not only a minimum but also a maximum.

31   Keywords: multi-component fuels; droplet evaporation; supercritical conditions; mixing transition

32   criterion; phase transition; molecular dynamics

33

34   1.   Introduction

35   With the current energy system for the world economy, fossil fuels, such as hydrocarbons, are widely

36   used [1]. The large amounts of emissions of greenhouse gases, such as CO_2 [2-4] and nitrogen oxides [5],

37   have made the problem of global warming more and more severe [6-10], and the issue of saving energy

38   has also attracted people's attention [9, 11]. To solve the energy crisis, improving the utilization efficiency

39   of fossil fuels is essential [12], in addition to exploring alternative and renewable energies [5, 13-17].

40   Achieving combustion of hydrocarbon fuels under high-pressure and high-temperature conditions is an

41   important measure to improve the efficiency and reduce emissions of power devices such as internal

42   combustion engines (ICEs) [18]. The actual hydrocarbon fuel used by engines is a complex mixture

43   containing hundreds of components [19, 20]. The evaporation process is a necessary step before the fuel

* Corresponding Author, Tel: +86 13811176872, E-mail: max@tsinghua.edu.cn

44   is burned, and has a significant impact on the combustion and emission formation processes [21-24].

45   Under low-pressure conditions, a sharp interface exists between ambient gases and liquid fuels because

46   of the surface tension, where the classic two-phase evaporation dominates the fuel-ambient gas mixing

47   process [25]. However, when the ambient condition in the combustion chamber exceeds the critical point

48   of the injected fuel, the fuel droplet surface will undergo a transition from the liquid state to a supercritical

49   state [18, 26]. Under this circumstance, the surface tension gradually decreases, resulting in the

50   disappearance of the vapor-liquid interface [27-29]. Dahms et al. [25] have reported that the one-phase

51   diffusion would dominate the process of fuel-ambient gas mixing instead of the classical two-phase

52   evaporation, due to the lack of intermolecular forces.

53   Different aspects of the evaporation of droplets under supercritical conditions have been reviewed

54   [30-33]. Nonetheless, a reliable criterion to decide the dominant mixing mode in the mixing process of

55   fuel-ambient gas, which is a fundamental question, has not been well established. Several theories and

56   methods used to determine whether the transition occurs or not have been proposed [34]. Among these,

57   the Knudsen number criterion [27] and the critical trajectory theory [35] are the most popular ones. The

58   first is based on the comparison between the mean free path of the molecules and the thickness of the

59   vapor-liquid interface. However, the theoretical analyses based on the Knudsen number are made under

60   the assumption of steady-state, which cannot accurately depict the dynamic transition process [36]. In the

61   critical trajectory theory, the transition process is evaluated through comparison between the apex of

62   vapor-liquid equilibrium (VLE) curves of the binary system and temperature-fuel fraction profiles of the

63   evaporation system. This method is applicable only if the critical point of the mixture is known, which

64   itself is another difficult unsolved problem, especially for multi-component fuels [37-40]. Falgout et al.

65   [38] concluded that the critical property of a mixture might be completely different from that of its

66   individual component，so it was almost impossible to estimate the VLE curves of nitrogen and the mixed

67 fuel accurately in their study. It is reasonable to draw the conclusion that any scheme based on calculation

68 of the critical point is not applicable for mixtures of multi-component fuels and ambient gases.

69   Remarkable differences are present between the evaporation process of a droplet in subcritical

70 conditions and that in supercritical conditions [41]. It is inappropriate to apply the traditional droplet

71 evaporation theory to supercritical conditions [26]. In addition, due to the inherent deficiency of CFD [33,

72 36], it is difficult to accurately calculate the critical properties of mixtures during the transition process.

73 In terms of experiments, the droplet evaporation process is usually studied by a droplet hanging test [22,

74 42-44]. However, due to the limitations of current experimental means, only macroscopic physical

75 quantities can be obtained through experiments, whose macroscopic nature leads to its failure to analyze

76 the supercritical transition behavior of the droplet in detail [26]. Molecular dynamics (MD) has been

77 increasingly applied to the study of droplet evaporation, avoiding the problems encountered in CFD

78 simulations and experiments [26, 45-47]. In MD simulations, no assumptions are required about the

79 physical processes to be simulated except potential models of intermolecular forces, and all

80 thermophysical properties are obtained by statistical methods. Consequently, the correct formulation and

81 application of force potential functions is crucial [48]. MD simulations can be performed to study the

82 detailed physical process under high pressures and/or high temperatures at atomic scales, thus resolving

83 the vapor-liquid interface thickness [47]. As a result, some researchers have studied the scale effect on

84 fuel evaporation using MD simulations [26, 36]. On the other hand, such simulations are computationally

85 very expensive and require supercomputing resources.

86   Most of the existing MD simulations of droplet evaporation are focused on subcritical conditions

87 [49-56] while studies under supercritical conditions are few and far inbetween [26, 57, 58] , especially for

88 complex hydrocarbon molecules [26]. This is because in the early days, it was difficult to simulate large

89 molecular systems due to the lack of force potential functions suitable for complex molecules and the lack

90 of sufficient computing power. Long et al. [56] studied the evaporation processes of argon droplets in

subcritical autogenous vapours, which did not involve supercritical cases. Kaltz et al. [58] found that when

oxygen droplets evaporated in hydrogen or helium environments, the critical pressure for transition was

much higher than that of pure oxygen. With the development of force potential functions and

improvement in computing power, it is now feasible to simulate the supercritical transition of complex

hydrocarbon fuels. MD simulations of the evaporation process of single-component hydrocarbon fuels

under supercritical conditions have been performed in recent years [26, 47]. Mo et al. [36] studied the

evaporation process of three types of single-component n-alkane liquid films in sub- and supercritical

nitrogen environments. They concluded that the transition occurred earlier with increasing ambient

temperature or ambient pressure. Xiao et al. [26] investigated the evaporation processes of n-dodecane

droplets in sub- and supercritical nitrogen environments, and obtained a regime diagram for sub- and

supercritical evaporation. However, these studies were focused on single-component fuels, leaving

questions unanswered about realistic fuels for engines.

So far, there have been very limited MD simulations of the evaporation process of multi-component

fuels due to the complexities in modeling and analysis. Chakraborty et al. [34] investigated supercritical

transitions of two-component fuel liquid films and discussed the changes in surface tension. Zhang et al.

[59] studied the evaporation process of a two-component n-alkane fuel film under sub- and supercritical

conditions and focused on the non-VLE effects under supercritical conditions. On the other hand,

surrogate fuels with multi-components (>2) have been shown to have a better match for the actual fuel

[60]. The evaporation process of multi-component droplets is much more complex when supercritical

transition is involved [61]. Establishing the MD approach for multi-component fuel evaporation to study

the VLE and supercritical transition process has important theoretical and practical significances [62, 63].

As has been reported [64], to have evaporation behaviors similar to those of real fuels, a surrogate

fuel should have at least three components. In this paper, the evaporation processes of a three-component

fuel droplet and a single-component (n-hexadecane) droplet under sub- and supercritical conditions were

investigated using MD simulations. The three-component fuel was composed of isooctane (5.3 wt%), n-dodecane (25.8 wt%) and n-hexadecane (68.9 wt%). This fuel was very close to Fuel C which consisted of isooctane (10 wt%), n-dodecane (30 wt%) and n-hexadecane (60 wt%) [65]. Fuel C had a similar distillation curve to Phillips #2 reference diesel fuel (DF2), as has been reported by Myong et al. [65]. The distillation curves of Fuel C and DF2 are shown in Fig. 1. Therefore, it was expected to have similar evaporation characteristics to those of commercial diesel fuels [65]. The n-hexadecane, the most representative single-component surrogate fuel for diesel [66], was also studied to provide comparisons. In recent years, researchers have found that the supercritical fluid region can still be divided into the gas-like phase region and the liquid-like phase region [67, 68], demonstrated in recent experiments [69]. In this paper, the local density distribution of the hydrocarbon fuel in evaporation systems was obtained from the Voronoi tessellation [70]. The objective of this paper is to investigate phase transition of multi-component hydrocarbon fuel droplets using MD simulations. A new criterion was proposed to determine whether the transition of the dominant mixing mode occurred or not for multi-component hydrocarbon fuels in supercritical conditions. A new parameter was proposed to estimate the phase transition speed of a hydrocarbon fuel. Effects of ambient temperature and ambient pressure on the mode transition were discussed. Moreover, effects of ambient conditions on phase transition speeds of different components were investigated. The dominant mixing mode maps on the P-T diagram for evaporation systems of pure n-hexadecane droplets and three-component fuel droplets were presented. Atomic-level insights into the differences between the mixing modes were obtained via the molecular distributions of both single-component and three-component fuel droplets.
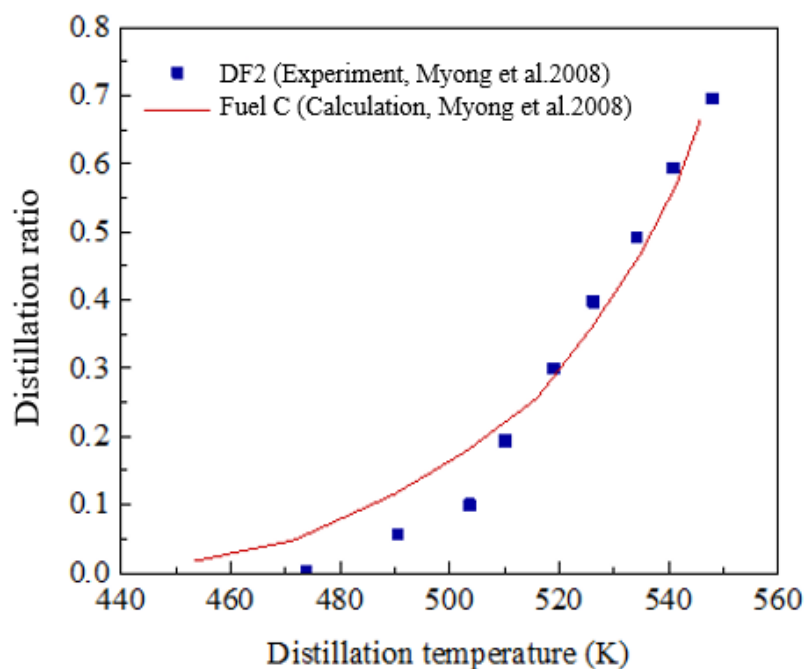
Fig. 1. Comparison of distillation curves of the two fuels. Redrawn based on [65].

2. Research methods

2.1 . Interatomic potentials

The MD simulations were carried out using the Large-scale Atomic/Molecular Massively Parallel Simulator (LAMMPS) [71], an open source MD code. In MD simulations, the molecular motion is calculated based on Newton's laws of motion. The calculation of intermolecular interaction forces is based on the potential model, whose choice is crucial [26]. Among the potential models for complex long-chain alkanes like n-dodecane, the United Atom Model (UAM) has been widely used because of its good balance between computational efficiency and precision [47]. The C-H bonds in complex alkanes are much longer and more powerful than the C-C bonds, which becomes the basis of the UAM [47]. An atom group, such as methyl (CH_3) or methylene (CH_2), is treated as a pseudo-atom [72]. As a result, alkane molecules are simplified into straight or branched molecules consisting of several associated atoms, as shown in Fig. 2.
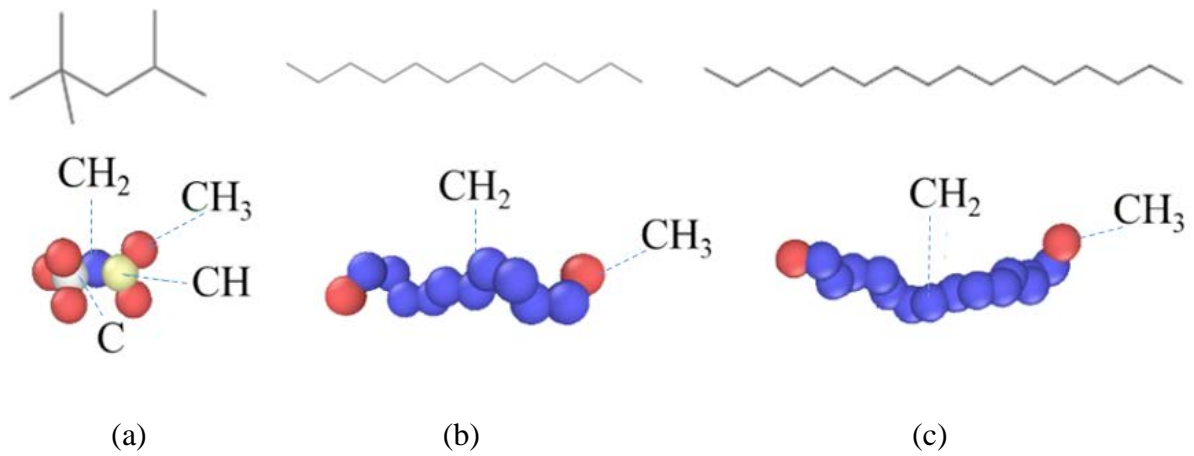
Fig. 2. The schematic diagram of the United Atom Model: (a) Isooctane, (b) n-Dodecane and (c) n-Hexadecane.

The Transferable Potentials for Phase Equilibria United Atom (TraPPE-UA) Model [73-75], which were shown to accurately produce fluid phase data of alkanes, were used to describe the interactions of fuel molecules. The non-bonded interaction between pseudo-atoms that are separated by more than three bonds or belong to two different molecules is described by the 12-6 Lennard-Jones potential:

$$U^{LJ}(r_{ij}) = 4\varepsilon_{ij}\left[\left(\frac{\sigma_{ij}}{r_{ij}}\right)^{12} - \left(\frac{\sigma_{ij}}{r_{ij}}\right)^{6}\right] \qquad (1)$$

where σ_{ij} is the size parameter, ε_{ij} is the energy parameter, and r_{ij} is the distance between the two interacting pseudo-atoms. The LJ parameters for identical pseudo-atoms are listed in Table 1 [74], where k_B is the Boltzmann constant. The LJ parameters for all unlike atoms are determined by the standard Lorentz-Berthelot combining rules [76], $\varepsilon_{ij} = \sqrt{\varepsilon_{ii} \cdot \varepsilon_{jj}}$ and $\sigma_{ij} = (\sigma_{ii} + \sigma_{jj})/2$.

Table 1. Lennard-Jones Parameters of the TraPPE-UA force field.

pseudo-atom	ε/k_B [K]	σ [Å]
CH_3	98	3.75
CH_2	46	3.95
CH	10	4.68
C	0.5	6.4

164   In the classical TraPPE-UA model, bond lengths between two connected pseudo-atoms are fixed.

165 However, LAMMPS does not provide an algorithm for fixing the bond length of a long-chain molecule

166 like n-dodecane or n-hexadecane. Therefore, the bond-stretching interaction is described by a harmonic

167 potential with a large force constant:

168 $U^s(r) = \frac{1}{2}k_b(r - r_0)^2$ (2)

169 where $r_0 = 1.54$ Å, and $k_b/k_B = 96508\ K \cdot Å^{-2}$, which are taken from the NERD model [77]. Previous

170 study has shown that this modification would not induce any difference in the simulation results of alkanes

171 [36]. Bond angle bending is also described by a harmonic potential:

172 $U^b(\theta) = \frac{1}{2}k_\theta(\theta - \theta_0)^2$ (3)

173 The motion of a dihedral angle, which is the interaction between two pseudo-atoms separated by three

174 bonds, is described by the OPLS (optimized potentials for liquid simulations) torsion potential [78]:

175 $U^t(\phi) = c_0 + c_1[1 + cos\phi] + c_2[1 - cos2\phi] + c_3[1 + cos3\phi]$ (4)

176 The bond bending and torsion parameters for alkanes are listed in Table 2 [74].

177   Table 2. Bond bending and torsion parameters for the TraPPE-UA force field.

Bond bending	θ_0 [°]		k_θ/k_B [K]	
CH_x-(CH_2)-CH_y	114		62500	
CH_x-(CH)-CH_y	112		62500	
CH_x-(C)-CH_y	109.47		62500	
Bond torsion	c_0/k_B [K]	c_1/k_B [K]	c_2/k_B [K]	c_3/k_B [K]
CH_x-(CH_2)-(CH_2)-CH_y (n-Alkanes)	0	335.03	-68.19	791.32
CH_x-(CH_2)-(CH)-CH_y (branched alkanes)	-251.06	428.73	-111.85	441.27
CH_x-(CH_2)-(C)-CH_y (branched alkanes)	0	0	0	461.29

178

179   To simplify calculations, each nitrogen molecule is regarded as two atoms connected by a

180 fixed bond length according to the SHAKE algorithm [79]. The interactions between the non-

181 bonded atoms are described by the potential function of 12-6 Lennard Jones. The size

182 parameter and the energy parameter are as follows: $\sigma_N = 0.332$ nm and $\varepsilon_N = 0.3026$ kJ / mol.

183 The bond length is fixed at 0.1106 nm.

184 2.2. Properties of fuels

185   Unlike lighter n-alkanes, n-hexadecane is prone to pyrolysis under high temperatures. Only a few

186 VLE data of n-hexadecane under the conditions of high-temperature were published. Lin et al. [80]

187 obtained the VLE data of the N_2-n-hexadecane (n-$C_{16}H_{34}$) system by the flow method. To estimate the

188 VLE data of the N_2–n-$C_{16}H_{34}$ binary system, theoretical calculations based on the combination of a real-

189 fluid equation of state (EoS) and the VLE theory are widely used [38, 81-84], and the experimental results

190 obtained by Lin et al. [80] are usually used to validate the theoretical model. Totally 26 data points were

191 published by Lin et al. [80], with the temperature range of 463-703 K and the pressure range of 2-25.5

192 MPa. In this work, the Peng-Robinson (PR) EoS [85] along with the classical mixing rules [86] was chosen

193 to establish a model for estimating the fluid properties of the system over the range of pressures and

194 temperatures of interest. This EoS is selected since it is computationally efficient and can give reasonably

195 accurate estimations of the VLE for non-polar mixtures [86]. Then, the model was used in combination

196 with the VLE theory to obtain the properties of the vapor state and the liquid state at given ambient

197 conditions (pressure and temperature).

198   The PR EoS can be written as

199 $$P = \frac{RT}{v-b} - \frac{a}{v(v+b)-v(v-b)} \tag{5}$$

200 where P is pressure, T is temperature, and v is molar volume. R is the universal gas constant (8.314 J/mol ·

201 K^{-1}). a is the attraction force and b is the volume parameter. For an individual component:

202 $$a = 0.457235\frac{R^2 T_c^2}{P_c} \cdot \alpha(T) \tag{6}$$

203 $$b = 0.077796\frac{RT_c}{P_c} \tag{7}$$

204 $$\alpha(T) = \left[1 + \kappa\left(1 - \sqrt{\frac{T}{T_c}}\right)\right]^2 \qquad (8)$$

205 where T_c is the critical temperature, and P_c is the critical pressure of a component. κ can be determined

206 by

207 $$\kappa = 0.3796 + 1.485\omega - 0.1644\omega^2 + 0.01667\omega^3 \qquad (9)$$

208 where ω is the acentric factor of a component. In the case of a mixture, the classical van der Waals mixing

209 rule is used to calculate these parameters:

210 $$a = \sum_i \sum_j x_i x_j a_{ij} \qquad (10)$$

211 $$b = \sum_i x_i b_i \qquad (11)$$

212 $$a_{ij} = (1 - \delta_{ij})\sqrt{a_i a_j} \qquad (12)$$

213 where x_i and x_j are the mole fractions of components i and j in the mixture, respectively. δ_{ij} is the binary

214 interaction parameter. For the N_2-n-$C_{16}H_{34}$ system, as discussed by García-Sánchez et al. [87], $\delta_{ij} =$

215 0.1816 can give good prediction results.

216   VLE conditions can be expressed as

217 $$T^V = T^L$$

218 $$P^V = P^L \qquad (13)$$

219 $$f_i^V = f_i^L$$

220 where superscript V denotes the vapor phase, L denotes the liquid phase.

221 f_i is the fugacity of component i, which can be determined by

222 $$f_i^V = y_i \phi_i^V$$

223 $$f_i^L = x_i \phi_i^L \qquad (14)$$

224 where ϕ_i is fugacity coefficient. Using the PR EoS, the analytical solutions of fugacity coefficients can

225 be expressed as

226 $\quad \ln \phi_i^L = \frac{b_i}{b^L RT}(pv^L - RT) - \ln\left[\frac{p}{RT}(v^L - b^L)\right] - \frac{a^L}{\sqrt{u^2-4w}b^L RT}\left[\frac{2\sum_j x_j a_{ij}}{a^L} - \frac{b_i}{b^L}\right] \times \ln\left[\frac{2v^L+(u+\sqrt{u^2-4w}b^L)}{2v^L+(u-\sqrt{u^2-4w}b^L)}\right]$ $\qquad$ (15)

227 $\quad \ln \phi_i^V = \frac{b_i}{b^V RT}(pv^V - RT) - \ln\left[\frac{p}{RT}(v^V - b^V)\right] - \frac{a^V}{\sqrt{u^2-4w}b^V RT}\left[\frac{2\sum_j y_j a_{ij}}{a^V} - \frac{b_i}{b^V}\right] \times \ln\left[\frac{2v^V+(u+\sqrt{u^2-4w}b^V)}{2v^V+(u-\sqrt{u^2-4w}b^V)}\right]$
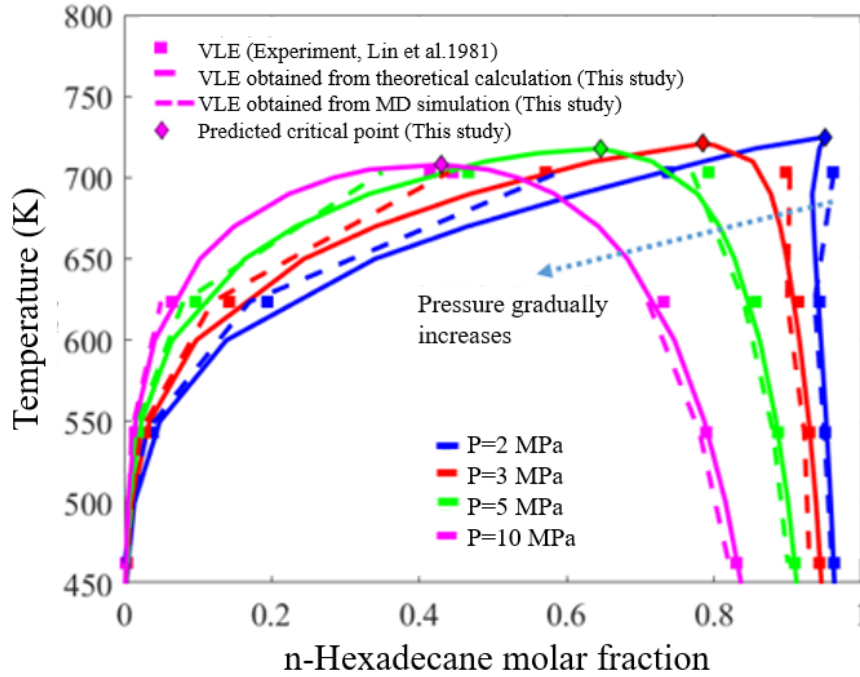
228

229   **Fig. 3.** VLE diagram of the nitrogen–n-hexadecane binary system. The experimental data are from [80].

230   The VLE curves obtained by theoretical calculations (EoS) under various pressures are shown in Fig.

231   2 in the form of a temperature-composition (T-x) phase diagram, along with experimental data taken from

232   Lin et al. [80]. The VLE calculations by MD simulations were also performed, and the obtained data were

233   plotted in Fig. 1. We can see from the figure that results from theoretical calculations are basically

234   consistent with those from experiments under all conditions. Calculation results obtained by MD

235   simulation can also give a fairly good prediction for the critical point of the binary mixture.

236   The characteristics of supercritical transition of a fuel rely heavily on its critical point. A theoretical

237   method based on empirical equations [88, 89] was used to estimate the critical point of the three-

238   component fuel. The estimation equation of the critical temperature of a simple mixture was given by Li

239   et al. [88], which can be expressed as

240 $$T_{c,m} = \sum_{i=1}^{n} \theta_i T_{c,i} \qquad (16)$$

241 where $T_{c,i}$ and θ_i are the critical temperature and the volumetric fraction of the ith component,

242 respectively. The later can be expressed as $\theta_i = (x_i V_{c,i})/(\sum_{i=1}^{n} x_i V_{c,i})$, where x_i and $V_{c,i}$ are the mole

243 fraction and critical molar volume of the ith component, respectively. The estimation equation of critical

244 pressure of a mixture was proposed by Kreglewski et al. [89], which can be expressed as

245 $$P_{c,m} = P_{pc}\left[1 + (5.808 + 4.93\omega_m)\frac{T_{c,m} - T_{pc}}{T_{Pc}}\right] \qquad (17)$$

246 where T_{pc} is the pseudo critical temperature, P_{pc} is the pseudo critical temperature and the pseudo critical

247 pressure of a mixture, and ω_m is the mean acentric factor. They can be expressed as the molar averages

248 of all individual components:

249 $$T_{pc} = \sum_{i=1}^{n} x_i T_{c,i}, P_{pc} = \sum_{i=1}^{n} x_i P_{c,i} \text{ and } \omega_m = \sum_{i=1}^{n} x_i \omega_i.$$

250 The estimated critical properties (including critical temperature T_c and critical pressure P_c) of the

251 three-component fuel, as well as that of its individual component, are shown in Table 3.

252 Table 3. Critical points of the fuel.

	T_c [K]	P_c [MPa]
isooctane	544	2.57
n-dodecane	658	1.81
n-hexadecane	722	1.4
3-component fuel	697	1.89

253

254 2.2 . Simulation configurations

255 The evaporation of a single suspended fuel droplet surrounded by nitrogen ambient was considered

256 in the present study. The initial configuration of the system is shown in Fig. 3. Before the simulations of

257 evaporation of droplets in nitrogen, simulations of the fuel droplet and the nitrogen ambient were

258 performed separately using the canonical ensemble (NVT, which means constant atom number N,

259   constant volume V, and constant temperature T) [36]. As both the fuel and the ambient gas reached their

260   own thermodynamic equilibrium state, they were combined together, with the nitrogen molecules in the

261   center region of the simulation box deleted to avoid the overlap of molecules. The initial temperature of

262   the fuel was set to 363 K, close to that of the fuel in real engines before injection.

263   The size of the simulation box was 120 nm × 120 nm × 120 nm, and periodic boundary conditions

264   were used in all three dimensions. The simulations were performed using the micro-canonical ensemble

265   (NVE, which means constant atom number N, constant volume V, and constant energy E) [47]. The

266   region outside of the sphere with a radius of 40 nm was named "thermostat region", in which velocities

267   of the molecules were rescaled every time step using a speed reset method [47]. The translational

268   velocities of the molecules located in this region were rescaled every time step according to

269        $$v_i^{new} = v_i^{old} \sqrt{\frac{3Tk_B N_t}{2E_k}} \qquad\qquad (18)$$

270   where E_k indicates the total kinetic energy of the N_t atoms in the thermostat region, and T indicates

271   the target ambient temperature. k_B is the Boltzmann constant. As a result, the temperature of this region

272   could be kept at a constant target value. The initial ambient pressure was determined by a combination of

273   the initial ambient temperature and the initial number of nitrogen molecules in the simulation box.

274   Different from the ambient temperature, in NVE simulations, the ambient pressure could not be

275   automatically kept by the simulator, which can be solved well by choosing the suitable initial number of

276   nitrogen molecules in the system [47]. The number ranges of nitrogen molecules are shown in Table 4.

277   Moreover, a molecule was removed as one of its atoms entered the thermostat region, so that the influences

278   of vapor phase fuel molecules on the droplet evaporation process were eliminated [26]. In this case, the

279   evaporation of the droplet can be thought of as taking place in an infinite space [26]. It is worth mentioning

280   that the ambient pressure, together with the gradients of temperature and fuel molar fractions, may

281 decrease due to the ongoing evaporation of the droplet. However, the droplet accounts for less than 1% of

282 the volume of the simulation box, so these changes are negligible.

283

284 (a) (b)
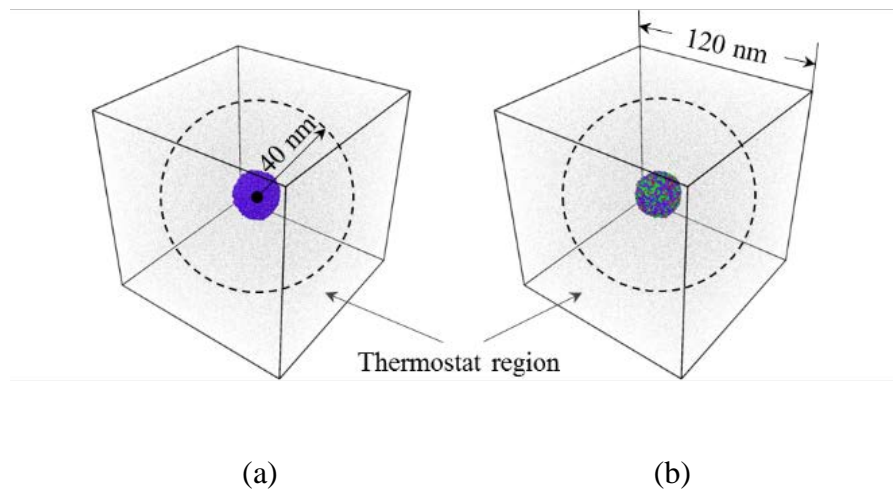
285 **Fig. 4.** Initial configurations: (a) A single-component fuel droplet, (b) A three-component fuel droplet.

286 Purple particles indicate n-hexadecane molecules, green particles indicate n-dodecane molecules and red

287 particles indicate isooctane molecules.

288 Initially, the single-component droplet and the three-component droplet contained 19,999 and 19,815

289 fuel molecules, forming initial diameters of 26.5 nm and 25.5 nm, respectively. Other details are

290 summarized in Table 4. In order to consider both subcritical and supercritical conditions [47], the target

291 ambient temperature and the target ambient pressure of simulations for two types of fuel droplets were

292 both 750-1200 K and 2-10 MPa, respectively. Considering typical operating conditions for a supercharged

293 diesel engine near the end of the compression stroke [47], the maximum ambient temperature (1200 K)

294 and the maximum ambient pressure (10 MPa) were chosen in this study. To take into account the

295 traditional evaporation behavior, the minimum ambient temperature (750K) and the minimum ambient

296 pressure (2 MPa) were selected in this study. The reduced ambient temperature T_r and the reduced ambient

297 pressure P_r are both calculated by dividing ambient values by critical values of fuel. The integral of the

298 equation of motion was carried out by the velocity-Verlet algorithm [90]. In all cases, the time step is 2.0

299 femtosecond. The total time steps for each simulation case varied with the droplet evaporation lifetime.

300   Table 4. Simulation details of single-component fuel droplets and three-component fuel droplets.

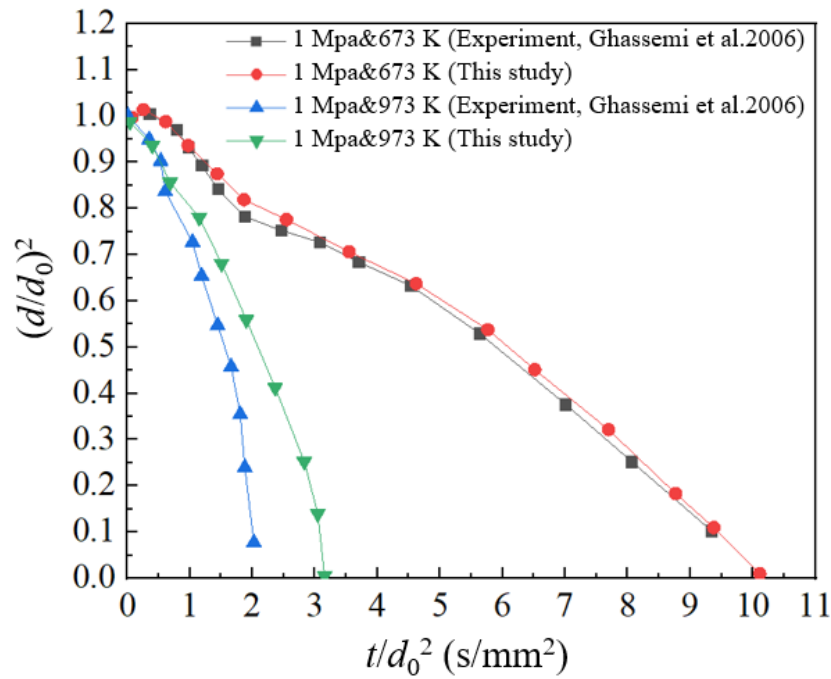|	Single-component droplet	Three-component droplet
Initial number of fuel molecules in the droplet	19,999 (n-hexadecane)	1830 (isooctane, 5.3 wt%) 5987 (n-dodecane, 25.8 wt%) 11998 (n-hexadecane, 68.9 wt%)
Initial droplet diameter, nm	26.5	25.5
Initial number of nitrogen molecules	205505 - 1585024	205709 - 1585230
Reduced ambient pressure	1.43 - 7.14	1.06 - 5.29
Reduced ambient temperature	1.04 - 1.6	1.08 - 1.72

301

302   The initial configuration mentioned above was validated by performing MD simulations of the

303 evaporation of a two-component fuel droplet, as shown in Fig. 5. Figure 6 shows the droplet evaporation

304 histories obtained by MD simulations, which is compared with the experimental results of Ghassemi et al.

305 [91]. The squared droplet diameter d^2 was normalized here by the squared initial droplet diameter d_0^2,

306 and time was also divided by d_0^2, to enable direct comparisons of the evaporation histories for different

307 droplets. In their experiments [91], the evaporation process of a two-component droplet composed of 50

308 vol.% n-heptane and 50 vol.% n-hexadecane was recorded by a high-speed camera, and the temporal

309 variations of the squared droplet diameter (d^2) were obtained. The evaporation histories of fuel droplets

310 under the ambient pressure of 1.0 MPa and ambient temperatures ranging from 673 K to 973 K could be

311 divided into two stages, which is induced by the obviously different evaporation characteristics of the two

312 components of the droplet [91]. In our simulations, initially the two-component droplet included 12218

313 n-heptane molecules (52 vol.%) and 5697 n-hexadecane molecules (48 vol.%), with an initial diameter of

314   22 nm. The temporal variations of d^2 during the evaporation process under the ambient pressure of 1.0

315   MPa and ambient temperatures of 673 K and 973 K are also shown in Fig. 6. It is evident that the d^2 curve

316   at 673 K shows an obvious two-stage phenomenon. At the higher ambient temperature (973 K), this two-

317   stage phenomenon is not so noticeable, which is caused by the faster temperature increase of the droplet.

318   The same trend was also observed in the studies of Ghassemi et al. [91], as shown in Fig. 6. It is worth

319   mentioning that the difference in the droplet evaporation lifetime obtained in two studies at the higher

320   temperature (973 K) is greater. As discussed in [92], in the experiment, the diameter of the droplet was

321   obtained from the photograph by image processing, whose accuracy was limited. Moreover, the

322   measurement of droplet diameter at the higher temperature (973 K) had a large error due to the influence

323   of fuel vapor [92]. Therefore, MD simulations were proved to be able to capture the general behaviors of

324   an evaporating multi-component droplet, despite the large gap between the scales investigated by these

325   two methods.
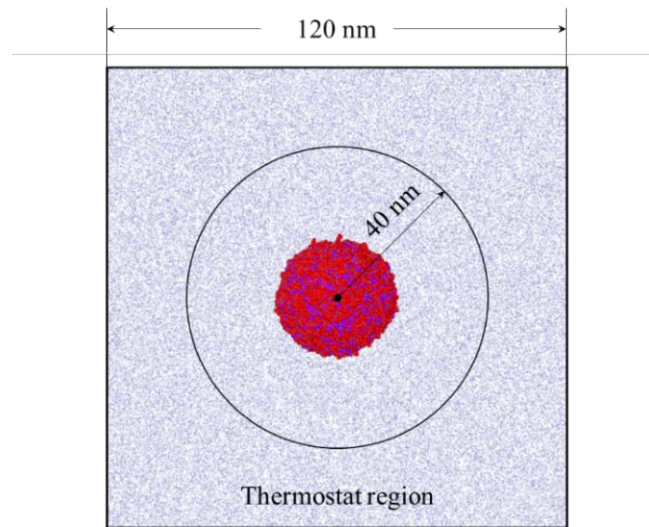
326

327   **Fig. 5.** Initial configuration of the two-component system. Purple particles indicate n-hexadecane

328   molecules and red particles indicate n-heptane molecules.

Fig. 6. Temporal variations of dimensionless square diameter $(d/d_0)^2$ of two-component droplets. The experiment data are from [91].

2.3. Voronoi tessellation

A certain space is divided into Voronoi cells according to the definition of the Voronoi tessellation. For a set of given points in a spatial domain, points in each Voronoi cell are closer to the given point in the Voronoi cell than any other points in the spatial domain [93]. Each cell could be regarded as a measure of volume of each particle [28]. To provide a clearer explanation, Fig. 7 shows a schematic diagram of Voronoi tessellation for particles on a plane. For a molecule system, the reciprocal of the Voronoi cell volume can be regarded as the local density of molecules, indicating the instantaneous local distributions of a certain molecule [28, 70, 94]. In fact, the Voronoi tessellation has been widely used in the density analyses of particle systems, and the inspections of local neighborhood relationships in the domains of physics and materials science [93].
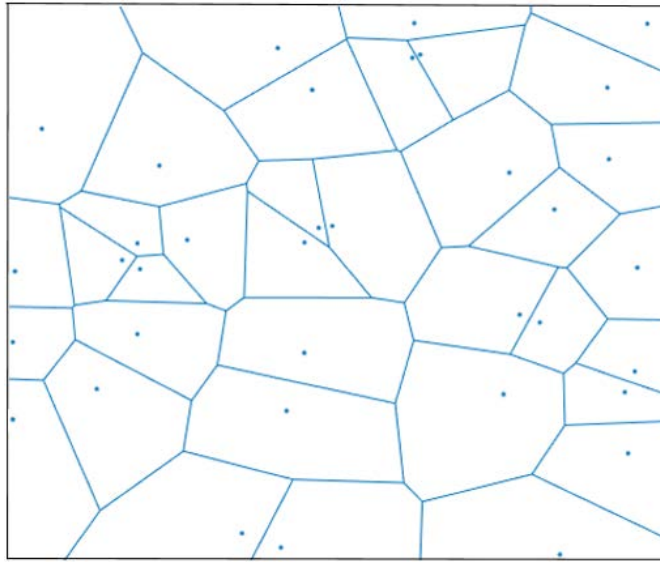
342

343   **Fig. 7.** The Voronoi tessellation for particles in a plane. The blue points indicate the given data.

344   3. Results and discussion

345   3.1. The macroscopic evaporation characteristics of multi-component droplets

346   The definitions of evaluation parameters for droplets are from [26]. The boundary of the droplet is

347   defined as the contour surface where the density is equal to the average of the maximum density and the

348   minimum density of the system . The diameter of the droplet is defined as that of a sphere of the same

349   volume as the droplet. Figure 8 shows temporal variations of dimensionless square diameter $(d/d_0)^2$ of

350   droplet, and time is also divided by d_0^2. The data points located in the range of 0.862 d_0^2 to 0.215 d_0^2

351   (corresponding to the initial droplet volume of 80% to 10%) are fitted by the method of least squares linear

352   fitting, and the slope of the fitting straight line is regarded as the evaporation rate constant k. The time

353   corresponding to the intersection point of the fitting line and the straight linear $d^2 = d_0^2$ is defined as the

354   initial heat-up time t_h. And the time corresponding to the intersection point of the fitting line and the

355   straight linear $d^2 = 0$ is defined as the droplet evaporation lifetime t_L. The relationship among them is

356   as follows:

357    $$t_L = t_h + \frac{d_0^2}{k}$$ (18)

358

359
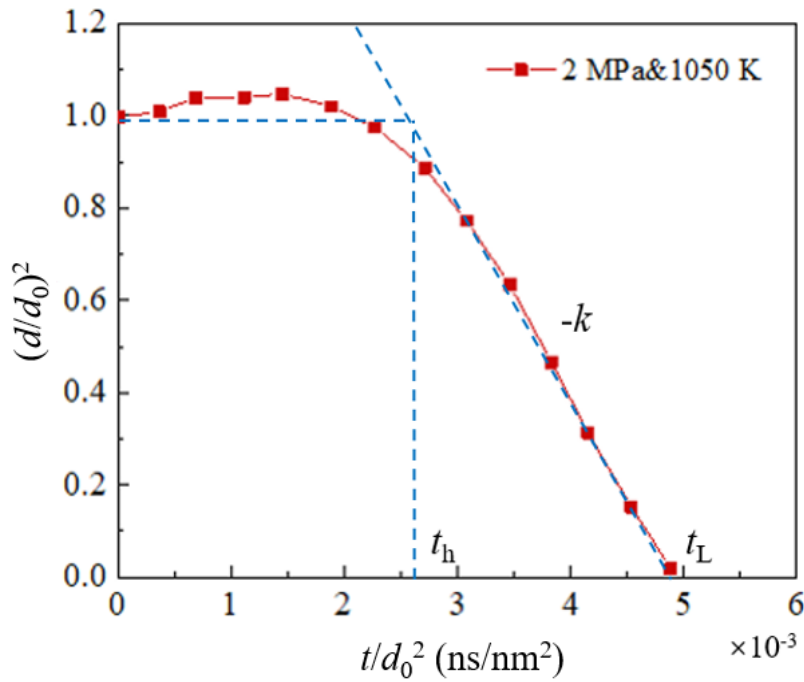
Fig. 8. The temporal variation of dimensionless square diameter $(d/d_0)^2$ of n-hexadecane droplet.

Figure 9 shows the temporal variations of $(d/d_0)^2$ of the single-component droplet and the three-component droplet, and time is also divided by d_0^2. The droplet size increases at the beginning of the evaporation, as shown in Fig. 9. This phenomenon has been attributed to the slow evaporation and the thermal expansion, revealed in previous studies [42]. The simulation results here suggest that the adsorption and dissolution of nitrogen molecules on the droplet may be additional reasons for it. Moreover, the normalized lifetimes of single-component droplets are longer than those of three-component droplets, especially under lower ambient pressures. The reason for this phenomenon will be discussed in the analysis of Fig. 10.

369
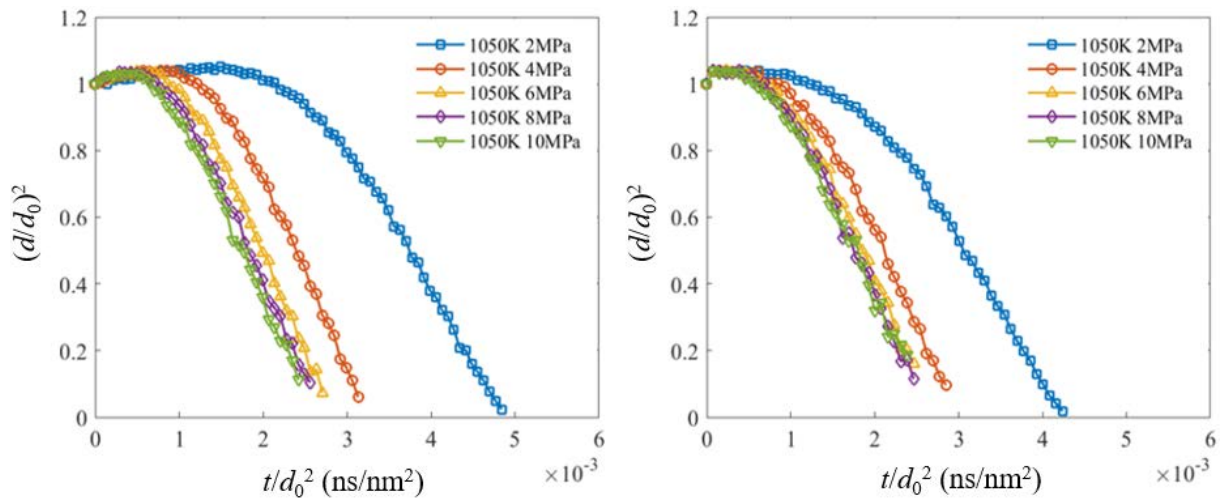
(a)   (b)

Fig. 9. Comparison of temporal variations of the dimensionless square diameters: (a) Single-component fuel droplets, (b) Three-component fuel droplets.

Figure 10 shows the change of the droplet evaporation lifetime t_L, initial heat-up time t_h and evaporation rate constant k as a function of ambient pressure, where the droplet evaporation lifetime and the initial heat-up time are normalized by d_0^2. With increasing ambient temperature, the temperature difference between fuel and ambient gas becomes larger, so the heat transfer is accelerated. Meanwhile, the gas phase diffusion coefficient also increases [26]. As seen from Fig. 10a, with increasing ambient temperature, the droplet evaporation lifetime decreases monotonously. Moreover, under the ambient temperatures investigated here, the droplet evaporation lifetime decreases monotonously with increasing ambient pressure. According to previous studies, including experiments [95, 96] and simulations [97], the droplet evaporation lifetime decreased monotonously under high temperatures (near T_c or exceed T_c) with increasing ambient pressure. The effect of decreasing latent heat of vaporization exceeded the combined effects of decreasing mass diffusivity and increasing boiling point of the fuel, leading to the decrease of droplet evaporation lifetime [26]. The temperatures studied in this paper are very high ($T > T_c$), so the present conclusion is consistent with existing ones [63, 95-98]. However, when the ambient pressure is

386 higher (P > 6 MPa), the effect of the decreasing latent heat of evaporation with increasing ambient

387 pressure is offset by the combined effect of the decreasing mass diffusivity, decreasing thermal

388 conductivity, and increasing boiling point of the fuel [26]. As a result, the droplet evaporation lifetime

389 hardly changes. The trend of the initial heat-up time t_h (Fig. 10b) with the ambient temperature and/or the

390 ambient pressure is basically consistent with that of the droplet evaporation lifetime t_L (Fig. 10a), which

391 is also consistent with the previous experimental results [42, 63]. The evaporation rate constant k increases

392 with increasing ambient temperature. However, k first increases and then decreases with increasing

393 ambient pressure. The trends are consistent with those obtained by experiments [42, 96]. The quantitative

394 results are compared below. Since no published similar results (including experimental results and

395 simulation results) are available to provide comparisons with those of the three-component droplet

396 selected in this paper, only the calculation results of n-hexadecane droplets are discussed here. The

397 experiments that the authors could find closest to the calculation cases of this paper come from Nomura

398 et al. [42]. The ambient pressures studied by them ranged from 1 MPa to 3 MPa, and the minimum ambient

399 pressure studied in this paper was 2 MPa. Therefore, the values of physical parameters at 2 MPa were

400 selected for comparison. The selected ambient condition of Nomura et al. [42] was 2 MPa and 773 K. The

401 ambient condition of 2 MPa and 750 K was selected for comparison in this paper. The fuel droplets were

402 both n-hexadecane, and the ambient gas was both nitrogen. Since the initial size of the droplet is different

403 (the experimental droplet diameter is 0.39 mm, and the simulated droplet diameter is 26.5 nm), all physical

404 quantities are divided by the square of the initial diameter of the droplet for convenience of comparison.

405 In the experiment of Nomura et al. [42], under the ambient condition of 2 MPa and 773 K, the droplet

406 evaporation rate constant k was 0.28 mm²/s, the normalized droplet evaporation life t_L/d_0^2 was 8.2 s/mm²,

407 and the normalized droplet initial heating time t_h/d_0^2 was 5.2 s/mm². In the present simulation, under the

408 ambient condition of 2 MPa and 750 K, the droplet evaporation rate constant k was 0.27 mm²/s , the

409 normalized droplet evaporation life t_L/d_0^2 was 7.5 s/mm², and the normalized initial heating time of the

410   droplet t_h/d_0^2 was 3.8 s/mm^2. It should be noted that the ambient temperature used in the simulation was

411   slightly lower than that used in the experiment. For k and t_L/d_0^2, the results of simulation and experiment

412   agree well. As for t_h/d_0^2, the results of the two are not quite consistent. This is because the data of d^2

413   obtained by the experiment fluctuates greatly, and the ranges of d^2 adopted for fitting k are different in

414   the simulation (using $0.862d_0^2$-$0.215d_0^2$) and experiment (using $0.5d_0^2$-$0.15d_0^2$), which will directly decide

415   the value of t_h/d_0^2. There is another interesting point worth discussing. As mentioned before, the

416   normalized lifetimes of single-component droplets are longer than those of three-component droplets,

417   especially under lower ambient pressures (P $\leqslant$ 6 MPa, Fig. 10a). The difference in the initial heat-up time

418   t_h between a single-component droplet and a three-component droplet is always greater than that in the

419   droplet evaporation lifetime t_L between the two droplets under lower pressures (P $\leqslant$ 6 MPa). Meanwhile,

420   the evaporation rate constant k of the three-component droplet is smaller than that of the single-component

421   droplet under almost all conditions. Equation (18) can be transformed as follows for an individual droplet:

422   $$\frac{t_L}{d_0^2} = \frac{t_h}{d_0^2} + \frac{1}{k} \tag{19}$$

423   Corresponding to equation (19), the $1/k$ term of the three-component droplet is larger than that of the

424   single-component droplet (Fig. 10c), but the t_L/d_0^2 term of the former is smaller under lower pressures (P

425   $\leqslant$ 6 MPa) (Fig. 10a), indicating that the shorter evaporation lifetime of the three-component droplet is

426   caused by t_h/d_0^2 term. In other words, the shorter evaporation lifetime of the three-component droplet,

427   compared with that of the single-component droplet, is caused by shorter initial heat-up time (Fig. 10b).

428   In the initial heat-up period, light components (isooctane and n-dodecane) of three-component droplets

429   evaporate first and take away the absorbed heat. As a result, the three-component droplet has a shorter

430   initial heat-up time, and a smaller size-increase as well, as shown in Fig. 9.

431

432

433   (a)   (b)   (c)
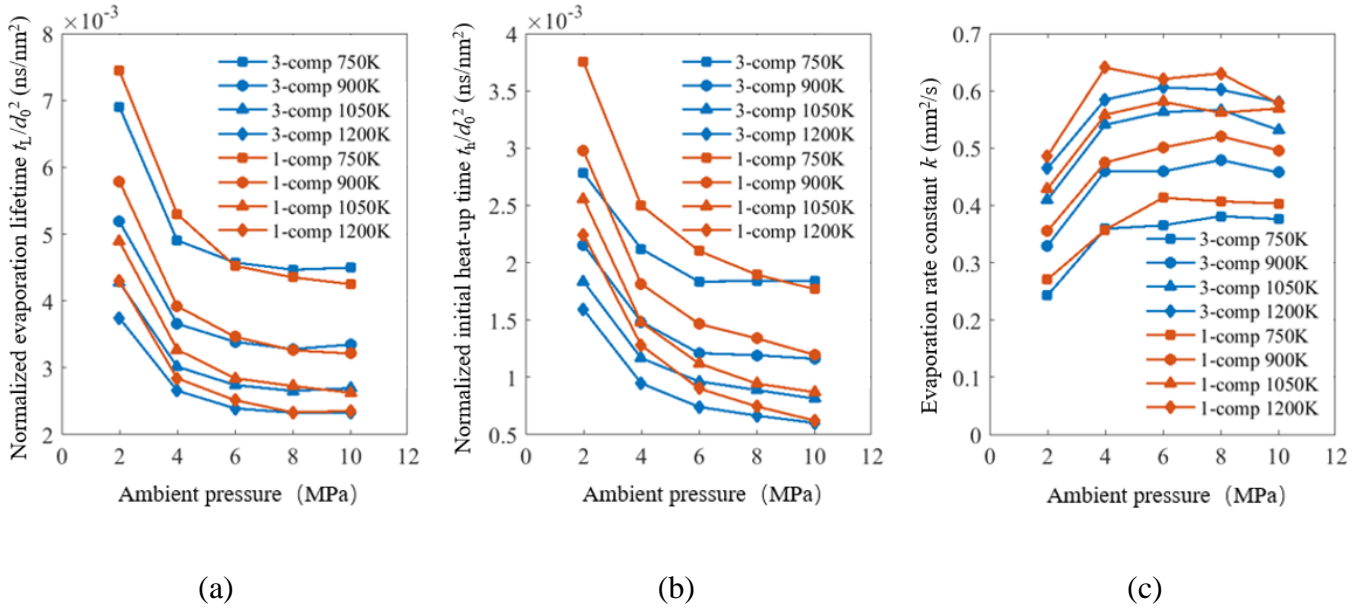
434   **Fig. 10.** Comparisons of evaporation evaluation parameters of two droplets: (a) Normalized evaporation

435   lifetime, (b) Normalized initial heat-up time and (c) Evaporation rate constant.

436   3.2. The phase transition and the dominant mixing mode transition of multi-component fuel droplets

437   In this section, the Voronoi tessellation method was used to calculate the local density

438   distributions of the two droplet evaporation systems. A new criterion was proposed to evaluate whether

439   single-component and multi-component fuels had realized the transition of the dominant mixing mode

440   from evaporation to diffusion in the mixing process of fuel-ambient gas. A new parameter was proposed

441   to evaluate the phase transition speed of the hydrocarbon fuel. The dominant mixing mode maps on the

442   P-T diagram for the evaporation systems of pure n-hexadecane droplets and three-component hydrocarbon

443   fuel droplets were presented.

444   3.2.1. The criterion for the transition of the dominant mixing mode
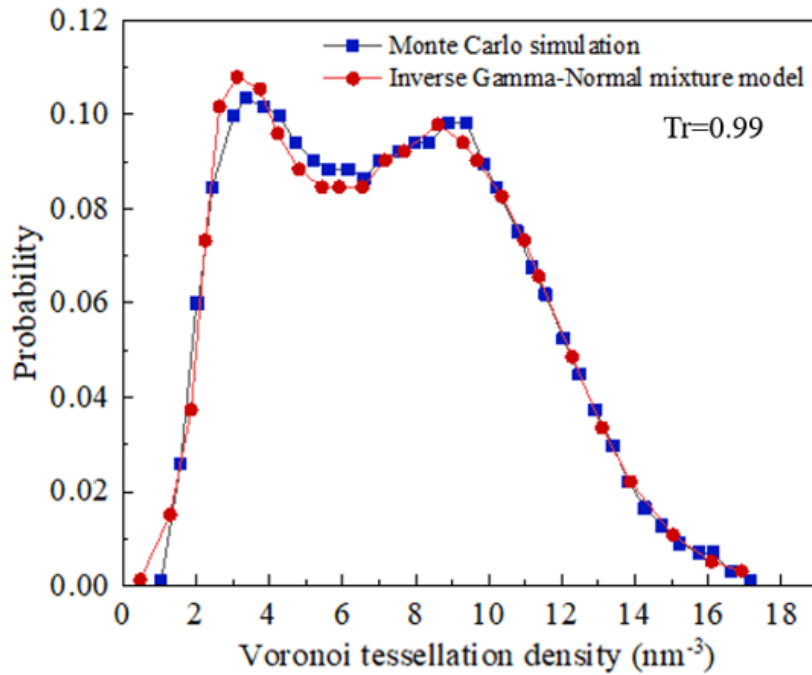
445   Figure 11 shows the local density distribution of n-hexadecane in the single-component droplet

446   evaporation system. The left and right peaks of the probability profile represent the vapor phase density

447 probability peak and the liquid phase density probability peak of n-hexadecane, respectively. The local

448 density distribution was fitted by the non-parametric fitting method with MATLAB. Four parameters (w_1,

449 w_2, h_1 and h_2) are defined, as shown in Fig. 11. w_1 represents the density difference corresponding to two

450 peak values when the two peak values of the probability profile are equal. w_2 represents the maximum

451 density difference of the n-hexadecane in the evaporation system. W, equal to w_1/w_2, represents the

452 dimensionless transition density. h_1 represents the probability value corresponding to the trough of the

453 probability profile. h_2 represents the probability value when the two peak values of the probability profile

454 are equal. H, equal to h_1/h_2, represents the dimensionless transition probability. Yoon et al. [70] obtained

455 the local density distribution of the supercritical CO_2 by the Voronoi tessellation, and proposed the

456 Inverse Gamma-Normal mixture model to fit it. Figure 12 shows the local density distribution of

457 CO_2 at $Tr = 0.99$. Based on a quantitative analysis of the local density distribution and the Inverse

458 Gamma-Normal mixture model of the CO_2 in supercritical state, and combined with the above analyses

459 in this paper, two critical values of $H_c = 0.85$ and $W_c = 0.35$ are adopted here. When diffusion instead of

460 evaporation becomes the dominant mode in the mixing process, the fuel and ambient gas both diffuse into

461 each other dramatically due to the large difference in density at the initial interface between them. After

462 that, the volume of Voronoi cell changes smoothly [28], and there is no longer a well-defined gas-liquid

463 interface. As a result, the transition between the two peaks of the probability profile will be smoother.

464 Besides, the two probability peaks will move close to each other [70], so the difference in the local

465 densities corresponding to the two peaks will decrease. In this case, for these two dimensionless

466 parameters, H will increase and W will decrease. For single-component fuels, when $W \leqslant W_c$ and $H \geqslant$

467 H_c, the dominant mode in the mixing process of fuel-ambient gas is diffusion, otherwise it is evaporation.

468 For multi-component fuels, the weighted average method is used to calculate the two parameters, and the

469 criterion to decide the dominant mixing mode in the mixing process of fuel-ambient gas is the same as

470 that of single-component fuels.
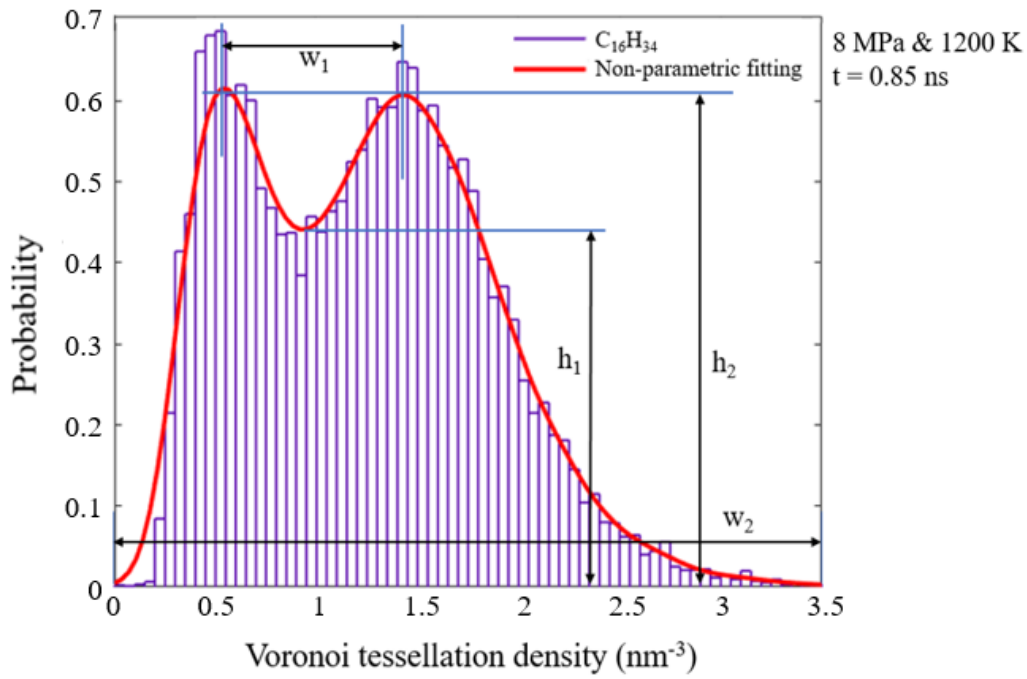
Fig. 11. The local density distribution of the n-hexadecane in the single-component droplet evaporation system.

Fig. 12. The local density distribution of CO_2. Redrawn based on [70].

477   3.2.2. The mechanism for the transition of the dominant mixing mode

478   Figures 13-16 show the changes of W and H parameters of n-hexadecane in single-component

479   droplets and individual component (n-hexadecane, n-dodecane, and isooctane) in three-component

480   droplets with ambient conditions, respectively. As shown in Figs. 13, W decreases and H increases with

481   increasing ambient pressure. However, W increases and H decreases slightly with increasing ambient

482   temperature. Variations of W and H of individual components of the three-component droplet (Figs. 14-

483   16) with ambient conditions are basically consistent with those of the single-component n-hexadecane

484   droplet (Fig. 13). The following conclusions can be drawn. With increasing ambient pressure, the density

485   differences between the vapor phase and the liquid phase decrease, and the dominant mode in the mixing

486   process of fuel-ambient gas may experience a transition from evaporation to diffusion. However, with

487   increasing ambient temperature, the density differences between the vapor phase and the liquid phase

488   increase, and evaporation gradually becomes the dominant mixing mode in the mixing process of fuel-

489   ambient gas.

490   The latest research from Banuti et al. [99] has provided the modified phase diagram of pure

491   substances, as shown in Fig. 17. The supercritical fluid region includes the whole regions of the liquid-

492   like phase and the gas-like phase, and part of the region of the ideal gas phase. Widom line, a finite length

493   line segment above the critical point, divides the supercritical phase into liquid-like one and gas-like one

494   [67]. Moreover, according to the previous study [100], similar to the pure fluid, a mutually miscible binary

495   mixture experiences a transition between liquid-like phase and gas-like phase in the region of supercritical

496   phase across a single Widom line. However, phase separation appears when transition occurs in the region

497   of supercritical phase for the immiscible binary mixture, and two Widom lines are present.

498   The following explanation is given in this paper. As isooctane, n-dodecane and n-hexadecane can be

499   miscible together, the ternary mixture could be treated as a pure fluid with a single Widom line in case of

500   transition in the supercritical region. Although nitrogen cannot be miscible with hydrocarbon fuel, it is

501   able to affect the phase transition of hydrogen fuel under supercritical conditions, that is, the length, shape

502   and position of the Widom line could be changed. The mixture of hydrocarbon fuel and nitrogen belongs

503   to type III [101], whose characteristic is that the critical pressure of the mixture system is getting higher

504   and the critical temperature is getting lower with increasing content of nitrogen. All ambient temperatures

505   investigated here (T ⩾ 750 K) are higher than critical temperatures of the two types of fuel (three-

506   component fuel: 697 K; single-component fuel: 722 K). Meanwhile, the critical temperature of the mixture

507   system, including the fuel droplet and nitrogen, is lower than that of the fuel itself because of the addition

508   of nitrogen.

509   Based on analyses above, there is no doubt that all ambient temperatures investigated here are higher

510   than the critical temperature of the two types of mixture systems. Several possible thermodynamic

511   pathways for phase transition of fuel are described below. The fuel is initially liquid. When the ambient

512   pressure is relatively higher and the ambient temperature is relatively lower, the final state of fuel will be

513   located in the region of the gas-like phase state or even the liquid-like phase state. Under this circumstance,

514   the thermodynamic path experienced by fuel is from the liquid phase to the supercritical gas-like phase or

515   the supercritical liquid-like phase. The density difference before and after phase transition is small (the

516   density of supercritical phase is slightly smaller than that of liquid phase, but much larger than that of gas

517   phase), and diffusion becomes the dominant mode in the mixing process of fuel-ambient gas.

518   Thermodynamic paths experienced by fuel are shown by the red dotted line with arrows in Fig. 17. When

519   the ambient temperature is relatively higher and the ambient pressure is relatively lower, the final state of

520   the fuel will be located in the region of the gas phase or even the ideal gas phase. When the thermodynamic

521   path experienced by fuel is from the liquid phase to the gas phase or the ideal gas phase, the density

522   difference between the initial phase state and the final phase state is larger, and evaporation will become

523   the dominant mode in the mixing process of fuel-ambient gas. Thermodynamic paths experienced by fuel

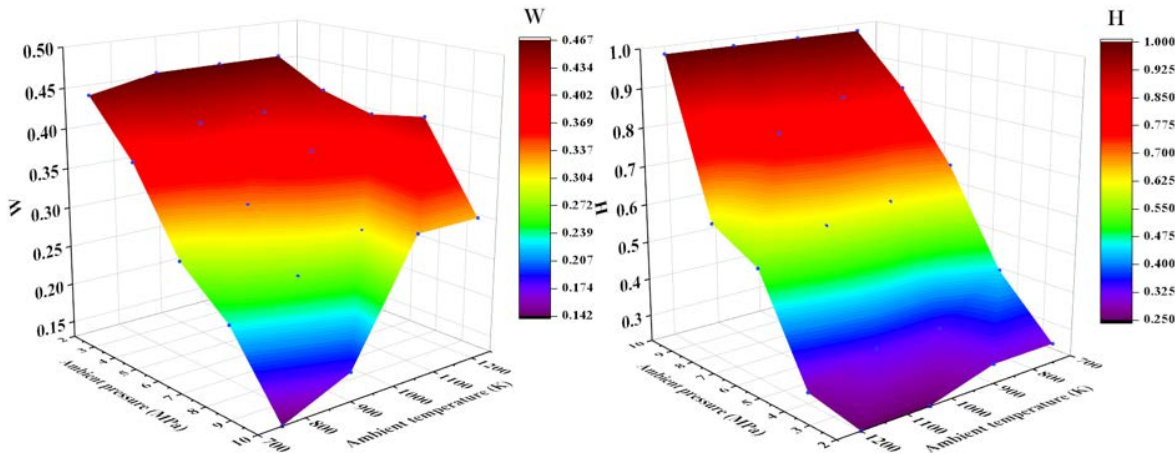524   are shown by the orange solid line with arrows in Fig. 17.

(a)   (b)
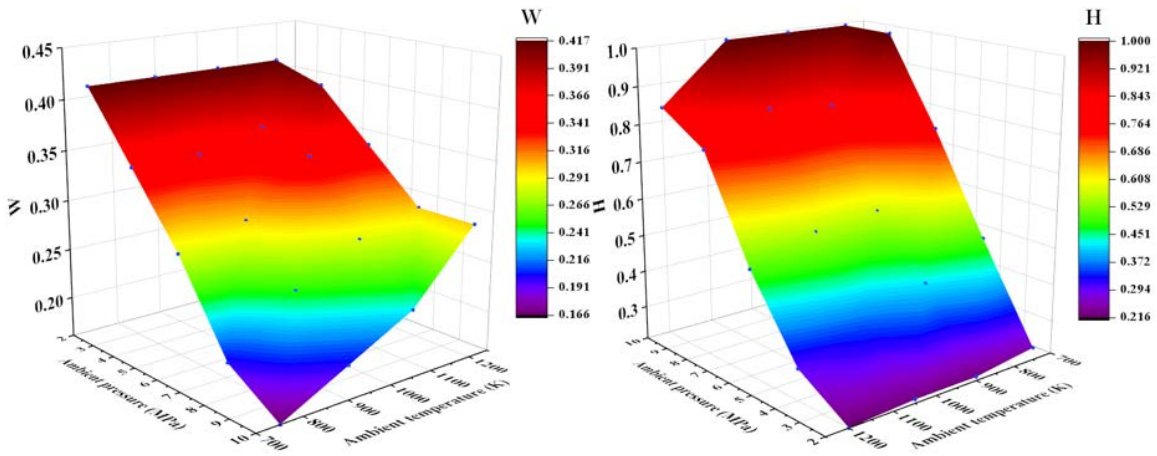
Fig. 13. Dimensionless transition density (W) and probability (H) diagrams of n-hexadecane in single-

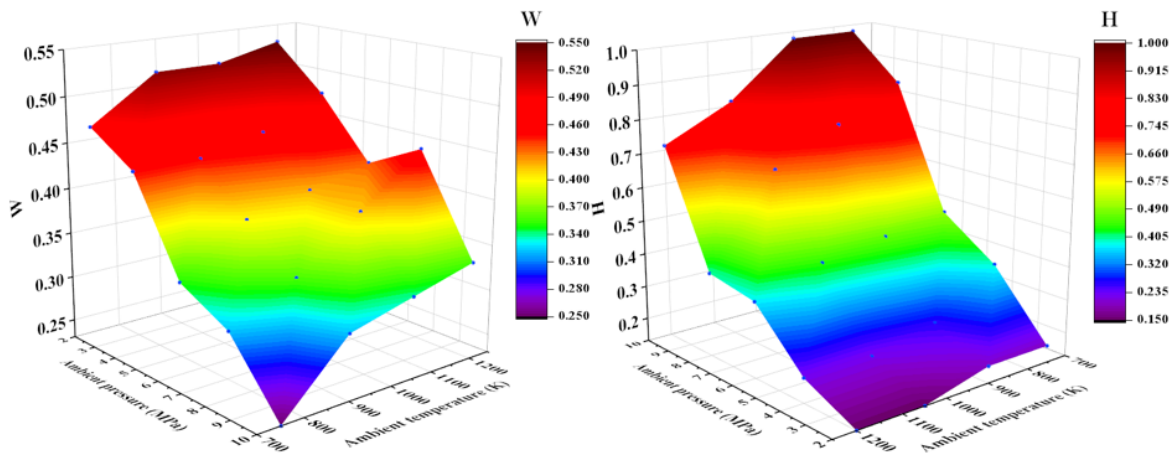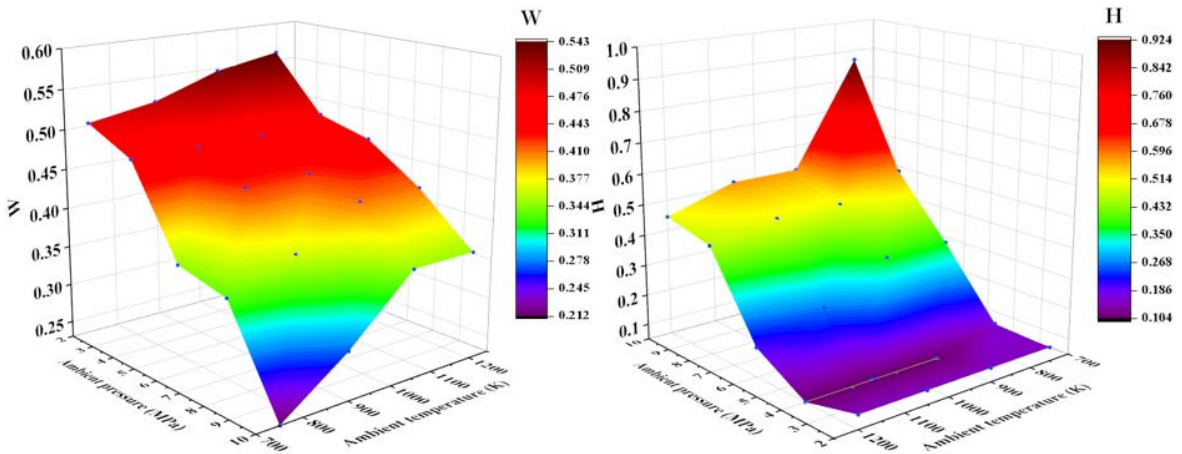component droplets: (a) W, (b) H. The blue points indicate the primary data.

(a)   (b)

Fig. 14. Dimensionless transition density (W) and probability (H) diagrams of n-hexadecane in three-

component droplets: (a) W, (b) H. The blue points indicate the primary data.

533

534 (a)   (b)

535 **Fig. 15.** Dimensionless transition density (W) and probability (H) diagrams of n-dodecane in three-

536 component droplets: (a) W, (b) H. The blue points indicate the primary data.

537

538 (a)   (b)

539 **Fig. 16.** Dimensionless transition density (W) and probability (H) diagrams of isooctane in three-

540 component droplets: (a) W, (b) H. The blue points indicate the primary data.
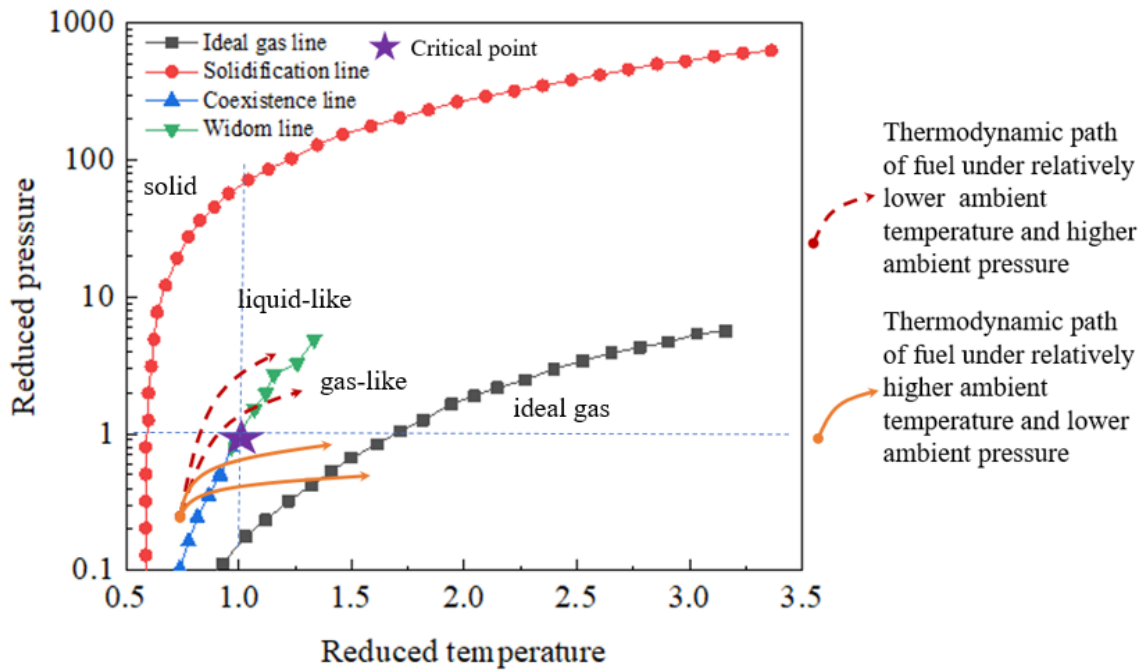
Fig. 17. Thermodynamic paths for liquid fuels. Redrawn based on [99].

3.2.3. Effects of ambient conditions on phase transition speeds of different components

The following definition is adopted in this paper. In the diagram of the local density distribution, the time when the two peak values of the probability profile are equal is defined as the vapor-liquid equal probability time $t_{pv = pl}$. Figures 18a-18d show the vapor-liquid equal probability time diagram of n-hexadecane of the single-component droplet and individual component (n-hexadecane, n-dodecane, and isooctane) of the three-component droplet, respectively. The magnitude of $t_{pv = pl}$ can be used to represent the phase transition speed. Under the same ambient pressure, $t_{pv = pl}$ gradually decreases with increasing ambient temperature, which means that the phase transition process is accelerated, consistent with previous studies [102]. However, the effect of pressure on the speed of phase transition is different from that of temperature. As shown in Figs. 18a–18c, when the ambient temperature remains constant, $t_{pv = pl}$ of n-hexadecane and n-dodecane decreases with increasing ambient pressure until 4 MPa. When the ambient pressure exceeds 4 MPa, $t_{pv = pl}$ of the fuel is basically unchanged with increasing ambient pressure. This means that the speed of phase transition remains constant, which is consistent with earlier conclusions

556 [26, 42]. However, the effect of pressure on the evaporation of isooctane (Fig. 18d) is different from that

557 of n-dodecane or n-hexadecane. For isooctane, $t_{pv\,=\,pl}$ increases monotonically with increasing ambient

558 pressure. This suggests that increasing ambient pressure might not be a good choice for speeding up the

559 mixing process of light component fuel (isooctane) and ambient gas. This finding agrees with the previous

560 study on n-heptane [103]. In their study, this was attributed to the decreasing mass diffusivity [103].

561

562 (a)   (b)

563

564 (c)   (d)
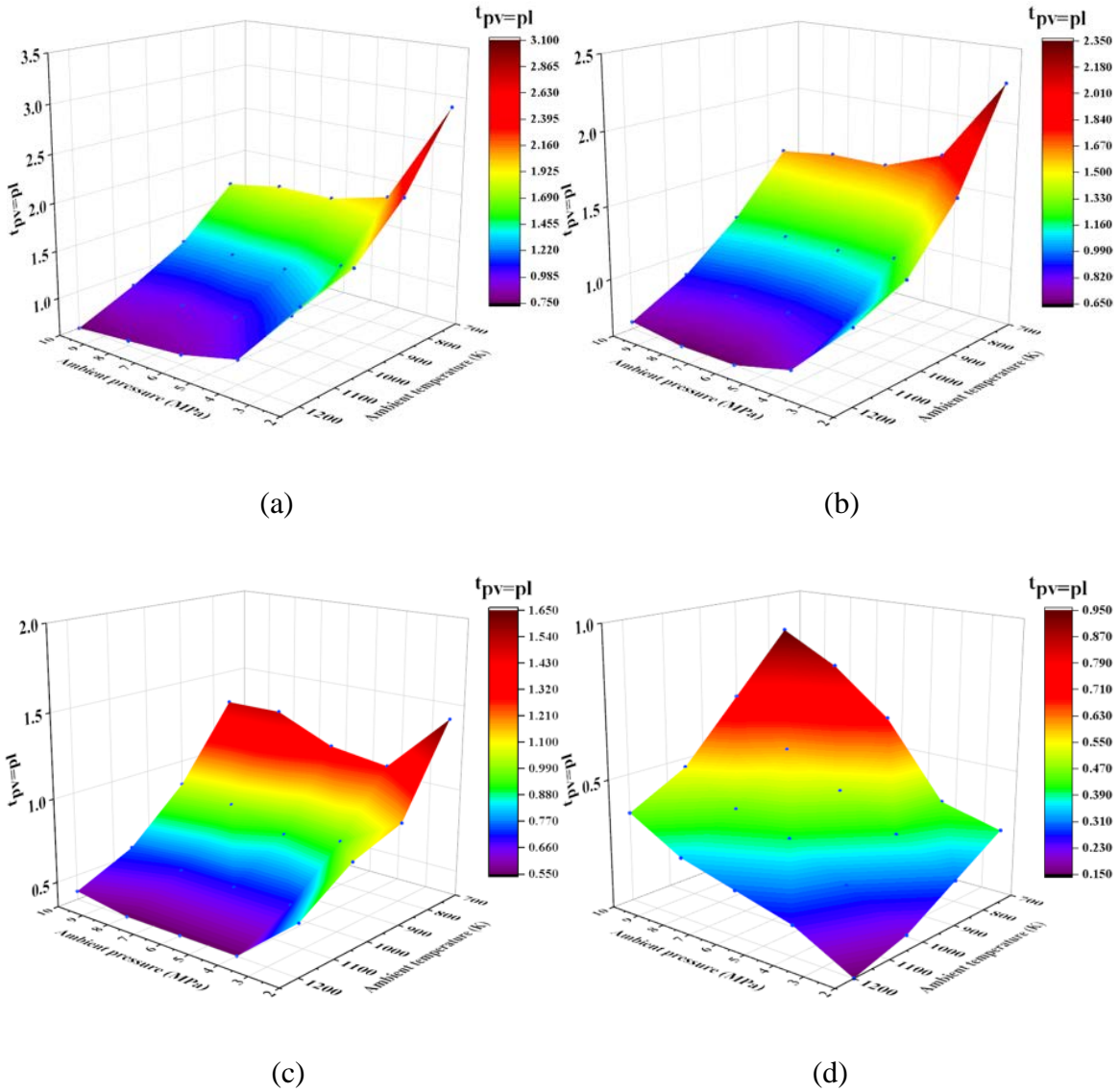
565 **Fig. 18.** Vapor-liquid equal probability time diagrams: (a) Single-component n-hexadecane droplets, (b)

566 n-Hexadecane in three-component droplets, (c) n-Dodecane in three-component droplets and (d)

567 Isooctane in three-component droplets. The blue points indicate the primary data.

568   3.2.4. The dominant mixing mode maps

569   According to the criterion proposed in Section 3.2.1, the dominant mixing mode maps on the P-T

570   diagram of pure n-hexadecane droplets, n-hexadecane in three-component fuel droplets and three-

571   component fuel droplets were obtained, as shown in Figs. 19a-19c respectively. According to the

572   comparison of Figs. 19a and 19b, the following conclusion can be drawn. For n-hexadecane in the three-

573   component fuel droplet, the maximum ambient temperature of the mixing zone dominated by diffusion is

574   higher under the same ambient pressure, compared with that of pure n-hexadecane droplet. For the three-

575   component fuel droplet, the minimum ambient pressure of the mixing zone dominated by diffusion is

576   higher than that of its individual component n-hexadecane, as shown in Figs. 19a and 19c. This is because

577   lighter components (isooctane and n-dodecane) have higher critical pressures compared with those of

578   heavy ones (n-hexadecane), increasing the overall critical pressure of the mixture.

579   Investigating the molecular distribution of supercritical fluid by Voronoi tessellation has been tried

580   before [28, 70]. The method of distinguishing the two dominant mixing modes based on the quantitative

581   Voronoi tessellation analysis was proposed in this paper, which is different from the two criterion

582   mentioned above [27, 35]. In previous reports [26, 27, 36], the minimum ambient temperature required

583   for fuel to undergo supercritical transition in ambient gas, that is, the critical mixing temperature, increases

584   with decreasing ambient pressure. Moreover, under a certain ambient pressure, as long as the ambient

585   temperature is not less than the critical mixing temperature, the supercritical transition always occurs. In

586   this study, it was found that the relationship between the critical mixing temperature and the ambient

587   pressure was more complicated when the supercritical transition of fuel occurred in ambient gas. Under a

588   certain ambient pressure, the ambient temperature where the fuel could undergo supercritical transition in

589   ambient gas had not only a minimum (the critical mixing temperature), but also a maximum. With

590   decreasing ambient pressure, the maximum value of the ambient temperature where the supercritical

591 transition could occur also decreased. So, this study provided a new insight into the process of supercritical
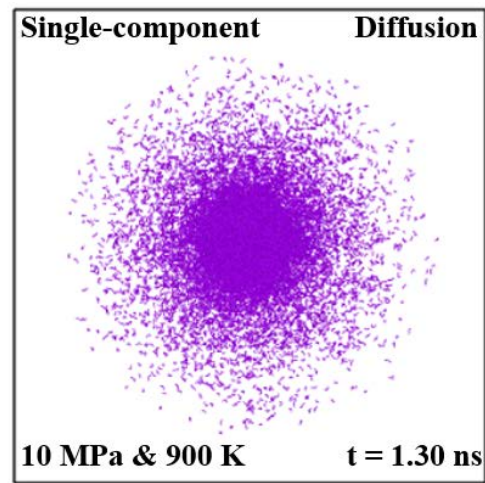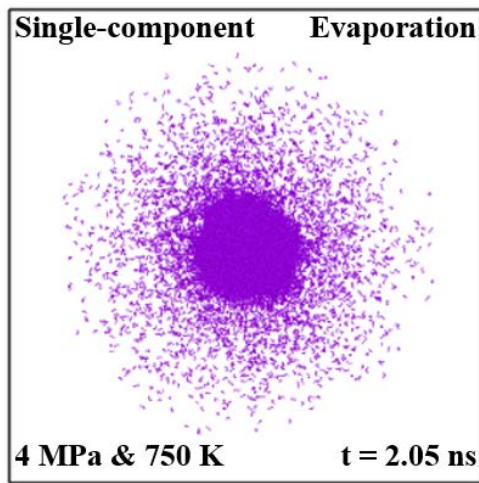
592 transition of fuel.
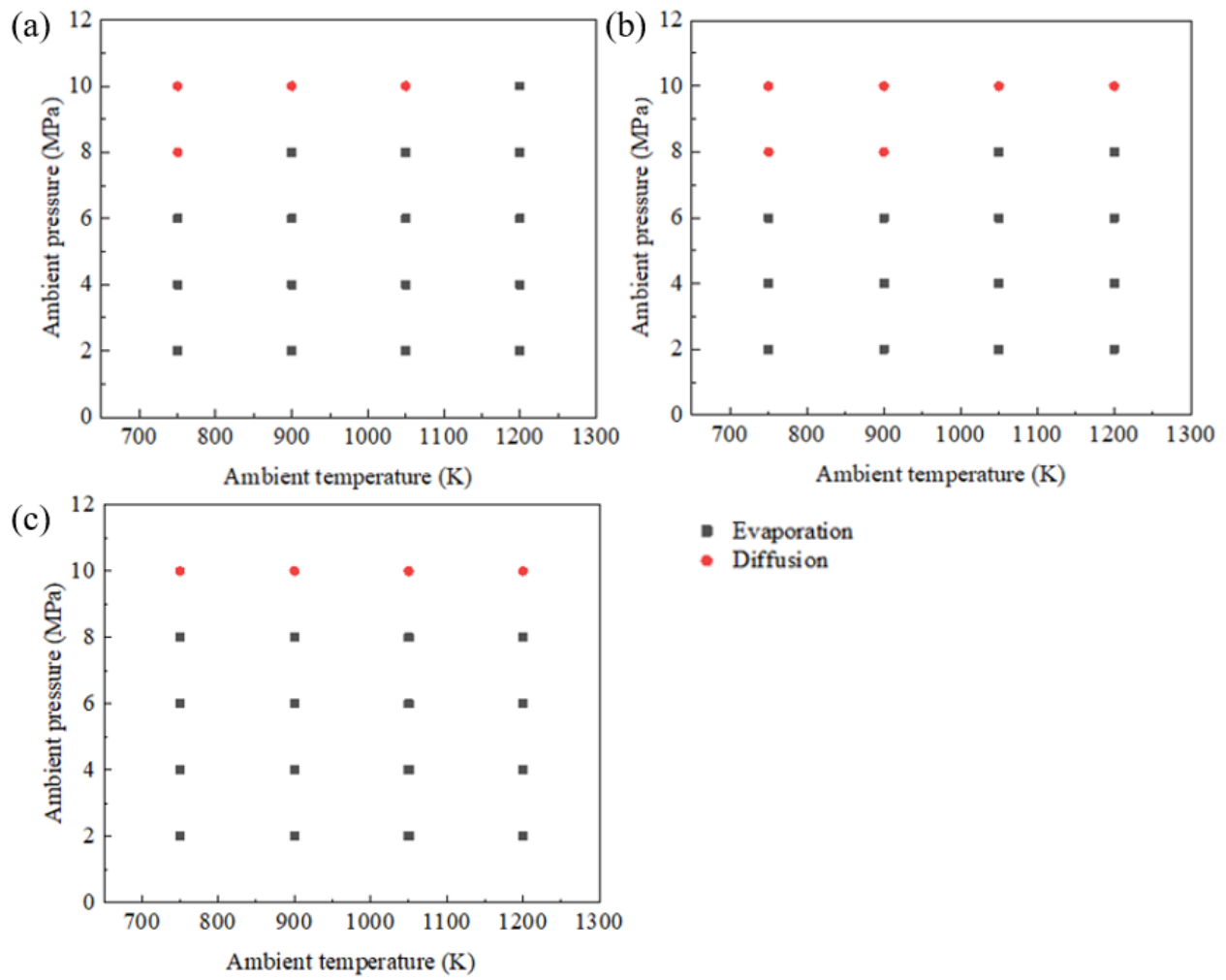
593

594 **Fig. 19.** The dominant mixing mode maps: (a) Pure n-hexadecane droplets, (b) n-Hexadecane in

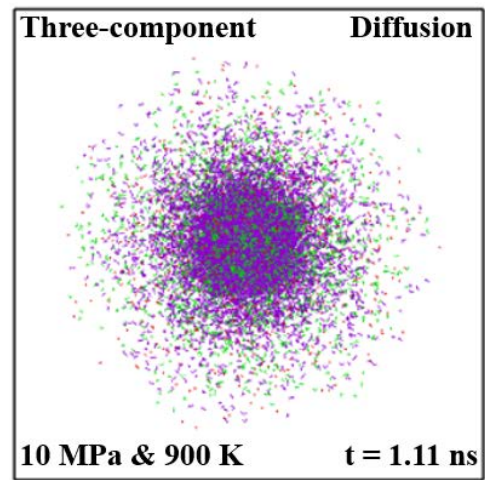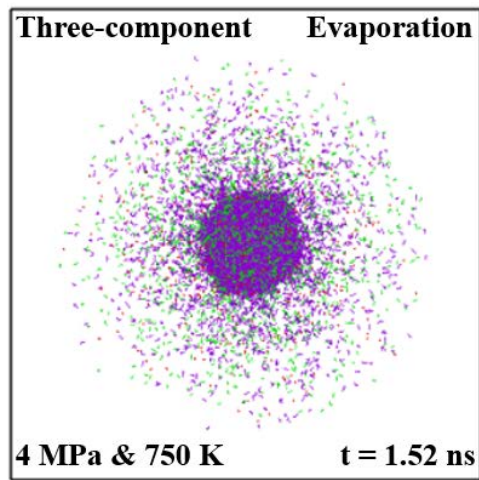595 three-component fuel droplets and (c) Three-component fuel droplets.

596

597

598

599

Fig. 20. Molecular distributions in the mixing process of single-component fuel droplets and three-component fuel droplets. Purple particles indicate n-hexadecane molecules, green particles indicate n-dodecane molecules and red particles indicate isooctane molecules.

According to the classification of Fig. 19, Fig. 20 shows molecular distributions in the mixing process of single-component fuel droplets and three-component fuel droplets in different dominant modes. In order to show the fuel phase transition process more clearly, only fuel molecules are included in the figure here, and nitrogen molecules are not shown. Figures 20a and 20b show the cases of single-component fuel

611   droplets in evaporation mode and diffusion mode, respectively, while Figs. 20c and 20d show the cases

612   of three-component fuel droplets in evaporation mode and diffusion mode, respectively. The moment of

613   the snapshot is determined according to the vapor-liquid equal probability time $t_{pv\,=\,pl}$ proposed in Section

614   3.2.3. The weighted average method is used to calculate the vapor-liquid equal probability time of the

615   three-component droplet. From the analysis in Section 3.2.2, when evaporation dominates the mixing

616   process of fuel droplets, the fuel transitions from the liquid phase to the gas phase or the ideal gas phase,

617   and the density of the fuel varies greatly before and after the phase transition. As shown in Figures 20a

618   and 20c, either droplet maintains a spherical shape, and the droplet boundary is sharp and clear. In the

619   interface between the liquid fuel and the ambient gas, the density gradient of the fuel is large. When

620   diffusion dominates the mixing process of fuel droplets, the fuel transitions from the liquid phase to the

621   supercritical gas-like phase or the supercritical liquid-like phase, and the density difference of the fuel

622   before and after the phase transition is small. As shown in Figures 20b and 20d, the contour of any droplet

623   is difficult to identify. Compared with the phase transition shown in Figs. 20a and 20c, the fuel after the

624   phase transition is denser and the thickness of the phase transition zone increases significantly, which

625   causes the density gradient of the fuel in this region to smaller (Figs. 20b and 20d). As a result, the phase

626   interface cannot be identified.

627   4. Conclusions

628   The evaporation process of the three-component hydrocarbon fuel (5.3 wt% isooctane, 25.8 wt% n-

629   dodecane and 68.9 wt% n-hexadecane) droplet in a nitrogen environment was studied using MD

630   simulations. As a comparison, the pure n-hexadecane droplet was also studied. Ambient conditions from

631   subcritical to supercritical were considered. The ambient pressure ranged from 2 MPa to 10 MPa and the

632   ambient temperature ranged from 750 K to 1200 K. Significant results of this study include:

633   1) Macroscopic droplet evaporation characteristics, such as the droplet evaporation lifetime, initial heat-

634   up time, and evaporation rate constant, were analyzed. The evaporation lifetime of the multi-component

635   droplet decreases with increasing ambient pressure and/or temperature. The change trend of droplet initial

636   heat-up time with ambient temperature and/or ambient pressure is basically consistent with that of the

637   droplet evaporation lifetime. The shorter evaporation lifetime of the three-component droplet is caused by

638   the shorter initial heat-up time, compared with that of the single-component droplet.

639   2) The new criterion suitable for both the single-component fuel and the multi-component fuel is one of

640   the main contributions of this paper. Based on the quantitative Voronoi tessellation analysis, a new

641   criterion, which is a combination of two dimensionless critical values of $H_c = 0.85$ and $W_c = 0.35$, was

642   proposed for the first time to determine the dominant mode in the mixing process of fuel-ambient gas. The

643   thermodynamic paths of the phase transition of fuel in the ambient gas were for the first time analyzed on

644   the revised phase diagram. Effects of ambient temperature and ambient pressure on the transition of the

645   dominant mixing mode were analyzed. When increasing ambient pressure or decreasing ambient

646   temperature, the density difference between the vapor and the liquid decreases, and the dominant mixing

647   mode gradually transitions from evaporation to diffusion. When the fuel experiences the phase transition

648   from the liquid phase to the supercritical liquid-like phase or the supercritical gas-like phase, the mixing

649   process of fuel-ambient gas is dominated by diffusion. However, when the fuel experiences the phase

650   transition from the liquid phase to the gas phase or the ideal gas phase, the mixing process of fuel-ambient

651   gas is dominated by evaporation.

652   3) A new parameter, namely the vapor-liquid equal probability time $t_{pv = pl}$, was proposed to evaluate the

653   phase transition speed of hydrocarbon fuels. The phase transition speed of each component of the three-

654   component fuel is accelerated with increasing ambient temperature. With increasing ambient pressure, the

655   phase transition speed of isooctane slows down, while that of n-dodecane or n-hexadecane increases. In

656   other words, increasing ambient pressure does not necessarily accelerate the phase transition, while

657   increasing ambient temperature increases the phase transition speed monotonically.

658   4) The dominant mixing mode maps on the P-T diagram for the evaporation systems of pure n-hexadecane

659   droplets and three-component hydrocarbon fuel droplets were presented. A major finding was that under

660   a certain ambient pressure, the ambient temperature where fuel could undergo supercritical transition in

661   the ambient gas had not only a minimum but also a maximum. With decreasing ambient pressure, the

662   maximum value of the ambient temperature where the supercritical transition could occur also decreased.

663   The addition of light components significantly increases the minimum pressure of the mixing zone

664   dominated by diffusion. In evaporation mode, the droplet boundary is sharp and clear. In the interface

665   between the liquid fuel and the ambient gas, the density gradient of the fuel is large. In diffusion mode,

666   the contour of the droplet is difficult to identify. The fuel after the phase transition is denser and the

667   thickness of the phase transition zone increases significantly, which causes the density gradient of the fuel

668   in this region to smaller. Future work could be to explore the relationship between the critical temperature

669   and the critical pressure of a multi-component fuel system under wider ambient conditions.

674   References

675   [1] Ul Hai I, Sher F, Zarren G, Liu H. Experimental investigation of tar arresting techniques and their
676   evaluation for product syngas cleaning from bubbling fluidized bed gasifier. Journal of Cleaner
677   Production 2019; 240. https://doi.org/10.1016/j.jclepro.2019.118239.
678   [2] Al-Juboori O, Sher F, Hazafa A, Kashif Khan M, Chen G Z. The effect of variable operating
679   parameters for hydrocarbon fuel formation from CO2 by molten salts electrolysis. Journal of CO2
680   Utilization 2020; 40. https://doi.org/10.1016/j.jcou.2020.101193.
681   [3] Ul Hai I, Sher F, Yaqoob A, Liu H. Assessment of biomass energy potential for SRC willow
682   woodchips in a pilot scale bubbling fluidized bed gasifier. Fuel 2019; 258.
683   https://doi.org/10.1016/j.fuel.2019.116143.

684   [4] Esteves AF, Soares OSGP, Vilar VJP, Pires JCM, Gonçalves AL. The Effect of light wavelength on
685   CO_2 capture, Biomass Production and Nutrient Uptake by Green Microalgae: A Step Forward on
686   Process Integration and Optimisation. Energies 2020; 13(2). https://doi.org/10.3390/en13020333.

687   [5] Razzaq L, Farooq M, Mujtaba MA, Sher F, Farhan M, Hassan MT, et al. Modeling viscosity and
688   density of ethanol-diesel-biodiesel ternary blends for sustainable environment. Sustainability 2020;
689   12(12). https://doi.org/10.3390/su12125186.

690   [6] Abu Hassan MH, Sher F, Zarren G, Suleiman N, Tahir AA, Snape CE. Kinetic and thermodynamic
691   evaluation of effective combined promoters for CO_2 hydrate formation. Journal of Natural Gas
692   Science and Engineering 2020; 78. https://doi.org/10.1016/j.jngse.2020.103313.

693   [7] Hansen S, Mirkouei A, Diaz LA. A comprehensive state-of-technology review for upgrading bio-oil
694   to renewable or blended hydrocarbon fuels. Renewable and Sustainable Energy Reviews 2020; 118.
695   https://doi.org/10.1016/j.rser.2019.109548.

696   [8] Sehar S, Sher F, Zhang S, Khalid U, Sulejmanović J, Lima EC. Thermodynamic and kinetic study of
697   synthesised graphene oxide-CuO nanocomposites: A way forward to fuel additive and photocatalytic
698   potentials. Journal of Molecular Liquids 2020; 313. https://doi.org/10.1016/j.enconman.2019.112266.

699   [9] Sher F, Pans MA, Sun C, Snape C, Liu H. Oxy-fuel combustion study of biomass fuels in a 20 kWth
700   fluidized bed combustor. Fuel 2018; 215: 778-86. https://doi.org/10.1016/j.fuel.2017.11.039.

701   [10] Duraisamy G, Rangasamy M, Govindan N. A comparative study on methanol/diesel and
702   methanol/PODE dual fuel RCCI combustion in an automotive diesel engine. Renewable Energy 2020;
703   145: 542-56. https://doi.org/10.1016/j.renene.2019.06.044.

704   [11] Al-Shara NK, Sher F, Iqbal SZ, Sajid Z, Chen GZ. Electrochemical study of different membrane
705   materials for the fabrication of stable, reproducible and reusable reference electrode. Journal of
706   Energy Chemistry 2020; 49: 33-41. https://doi.org/10.1016/j.jechem.2020.01.008.

707   [12] Zhang Y, Ran Z, Jin B, Zhang Y, Zhou C, Sher F. Simulation of particle mixing and separation in
708   multi-component fluidized bed using eulerian-eulerian method: A review. International Journal of
709   Chemical Reactor Engineering 2019; 17(11). https://doi.org/10.1515/ijcre-2019-0064.

710   [13] Al-Shara NK, Sher F, Yaqoob A, Chen GZ. Electrochemical investigation of novel reference
711   electrode $Ni/Ni(OH)_2$ in comparison with silver and platinum inert quasi-reference electrodes for
712   electrolysis in eutectic molten hydroxide. International Journal of Hydrogen Energy 2019; 44(50):
713   27224-36. https://doi.org/10.1016/j.ijhydene.2019.08.248.

[14] Nataša AK. Renewable energy: wind turbines, solar cells, small hydroelectric plants, biomass, and geothermal sources of energy. Journal of Energy and Power Engineering 2019; 13(4): 162-172. doi: 10.17265/1934-8975/2019.04.004.

[15] Senthilkumar G, Sajin JB, Yuvarajan D, Arunkumar T. Evaluation of emission, performance and combustion characteristics of dual fuelled research diesel engine. Environmental Technology 2020; 41(6): 711-8. https://doi.org/10.1080/09593330.2018.1509888.

[16] Sher F, Pans MA, Afilaka DT, Sun C, Liu H. Experimental investigation of woody and non-woody biomass combustion in a bubbling fluidised bed combustor focusing on gaseous emissions and temperature profiles. Energy 2017; 141: 2069-80. https://doi.org/10.1016/j.energy.2017.11.118.

[17] Sher F, Iqbal SZ, Liu H, Imran M, Snape CE. Thermal and kinetic analysis of diverse biomass fuels under different reaction environment: A way forward to renewable energy sources. Energy Conversion and Management 2020; 203. https://doi.org/10.1016/j.enconman.2019.112266.

[18] Wei W, Qin W, Yue M, Xie M. Numerical investigation on fuel injection into a multicomponent gaseous environment under trans/supercritical condition. Numerical Heat Transfer, Part A: Applications 2019: 1-18. https://doi.org/10.1080/10407782.2019.1677128.

[19] Szymkowicz PG, Benajes J. Single-cylinder engine evaluation of a multi-component diesel surrogate fuel at a part-load operating condition with conventional combustion. Fuel 2018; 226: 286-97. https://doi.org/10.1016/j.fuel.2018.03.157.

[20] Al Qubeissi M, Sazhin SS, Turner J, Begg S, Crua C, Heikal MR. Modelling of gasoline fuel droplets heating and evaporation. Fuel 2015; 159: 373-84. http://dx.doi.org/10.1016/j.fuel.2015.06.028.

[21] He X, Feng H, Liu Z, Wang H, Li X, Zeng F, et al. Numerical simulation of the evaporation characteristics of a dimethyl ether droplet in supercritical environment. Fuel 2020; 267. https://doi.org/10.1016/j.fuel.2020.117120.

[22] Ma Z, Li Y, Li Z, Du W, Yin Z, Xu S. Evaporation and combustion characteristics of hydrocarbon fuel droplet in sub- and super-critical environments. Fuel 2018; 220: 763-8. https://doi.org/10.1016/j.fuel.2018.02.073.

[23] Liu F, Gao Y, Zhang Z, He X, Wu H, Zhang C, et al. Study of the spray characteristics of a diesel surrogate for diesel engines under sub/supercritical states injected into atmospheric environment. Fuel 2018; 230: 308-18. https://doi.org/10.1016/j.fuel.2018.05.050.

[24] Yi P, Jia M, Long W, Qiao L, Yang T, Feng L. Evaporation of pure and blended droplets of diesel and alcohols (C2–C9) under diesel engine conditions. Numerical Heat Transfer, Part A: Applications 2017; 71(3): 311-26. https://doi.org/10.1080/10407782.2016.1264749.

[25] Dahms RN, Manin J, Pickett LM, Oefelein JC. Understanding high-pressure gas-liquid interface phenomena in Diesel engines. Proceedings of the Combustion Institute 2013; 34(1): 1667-75. https://doi.org/10.1016/j.proci.2012.06.169.

[26] Xiao G, Luo KH, Ma X, Shuai S. A molecular dynamics study of fuel droplet evaporation in sub- and supercritical conditions. Proceedings of the Combustion Institute 2019; 37(3): 3219-27. https://doi.org/10.1016/j.proci.2018.09.020.

[27] Dahms RN, Oefelein JC. On the transition between two-phase and single-phase interface dynamics in multicomponent fluids at supercritical pressures. Physics of Fluids 2013; 25. https://doi.org/10.1063/1.4820346.

[28] Rahmani F, Weathers T, Hosangadi A, Chiew YC. A non-equilibrium molecular dynamics study of subcritical, supercritical and transcritical mixing of liquid-gas systems. Chemical Engineering Science 2020; 214. https://doi.org/10.1016/j.ces.2019.115424.

[29] Crua C, Manin J, Pickett LM. On the transcritical mixing of fuels at diesel engine conditions. Fuel 2017; 208: 535-48. http://dx.doi.org/10.1016/j.fuel.2017.06.091.

[30] Givler S D, Abraham J. Supercritical droplet vaporization and combustion studies. Progress in Energy and Combustion Science 1996; 22: 1-28.

[31] Chiu H H. Advances and challenges in droplet and spray combustion. I. Toward a unified theory of droplet aerothermochemistry. Progress in Energy and Combustion Science 2000; 26: 381–416.

[32] Bellan J. Supercritical (and subcritical) fluid behavior and modeling: drops, streams, shear and mixing layers, jets and sprays. Progress in Energy and Combustion Science 2000; 26: 329–66.

[33] Yang V. Modeling of supercritical vaporation,mixing,and combustion process in liquid-fueled processes in liquid-fueled propulsion systems. Proceedings of the Combustion Institute 2000; 28: 925–42.

[34] Chakraborty S, Qiao L. Molecular investigation of sub-to-supercritical transition of hydrocarbon mixtures: Multi-component effect. International Journal of Heat and Mass Transfer 2019; 145. https://doi.org/10.1016/j.ijheatmasstransfer.2019.118629.

[35] Heidemann R A, Khalil A M. The calculation of critical points. AIChE Journal 1980; 26(5): 769-79.

[36] Mo G, Qiao L. A molecular dynamics investigation of n-alkanes vaporizing into nitrogen: transition from subcritical to supercritical. Combustion and Flame 2017; 176: 60-71. http://dx.doi.org/10.1016/j.combustflame.2016.09.028.

[37] Dahms RN, Oefelein JC. Liquid jet breakup regimes at supercritical pressures. Combustion and Flame 2015; 162(10): 3648-57. http://dx.doi.org/10.1016/j.combustflame.2015.07.004.

778 [38] Falgout Z, Rahm M, Sedarsky D, Linne M. Gas/fuel jet interfaces under high pressures and
779   temperatures. Fuel 2016; 168: 14-21. http://dx.doi.org/10.1016/j.fuel.2015.11.061.

780 [39] Wensing M, Vogel T, Gotz G. Transition of diesel spray to a supercritical state under engine
781   conditions. International Journal of Engine Research 2015; 17(1): 108-19.
782   https://doi.org/10.1177/1468087415604281.

783 [40] Xin N, Liu Y, Guo X, Liu X, Zhang Y, He M. Determination of critical properties for binary and
784   ternary mixtures containing propanol and alkanes using a flow view-type apparatus. The Journal of
785   Supercritical Fluids 2016; 108: 35-44. http://dx.doi.org/10.1016/j.supflu.2015.10.010.

786 [41] Sazhin SS. Modelling of fuel droplet heating and evaporation: Recent results and unsolved problems.
787   Fuel 2017; 196: 69-101. http://dx.doi.org/10.1016/j.fuel.2017.01.048.

788 [42] Nomura H, Murakoshi T, Suganuma Y, Ujiie Y, Hashimoto N, Nishida H. Microgravity experiments
789   of fuel droplet evaporation in sub- and supercritical environments. Proceedings of the Combustion
790   Institute 2017; 36(2): 2425-32. http://dx.doi.org/10.1016/j.proci.2016.08.046.

791 [43] Dai M, Wang J, Wei N, Wang X, Xu C. Experimental study on evaporation characteristics of
792   diesel/cerium   oxide   nanofluid   fuel   droplets.   Fuel   2019;   254.
793   https://doi.org/10.1016/j.fuel.2019.115633.

794 [44] Wang J, Huang X, Qiao X, Ju D, Sun C. Experimental study on effect of support fiber on fuel droplet
795   vaporization at high temperatures. Fuel 2020; 268. https://doi.org/10.1016/j.fuel.2020.117407.

796 [45] Holyst R, Litniewski M, Jakubczyk D. Evaporation of liquid droplets of nano- and micro-meter size
797   as a function of molecular mass and intermolecular interactions: experiments and molecular dynamics
798   simulations. Soft Matter 2017; 13(35): 5858-64. https://doi.org/10.1039/ c7sm00804j.

799 [46] Stubbs JM. Molecular simulations of supercritical fluid systems. The Journal of Supercritical Fluids
800   2016; 108: 104-22. http://dx.doi.org/10.1016/j.supflu.2015.10.027.

801 [47] Xiao G, Luo KH, Ma X, Shuai S. Liquid fuel evaporation under supercritical conditions.
802   Communications   in   Computational   Physics   2018;   23(4):   1241-62.
803   http://dx.doi.org/10.4208/cicp.OA-2016-0252.

804 [48] Janzen T, Fingerhut R, Heinen M, Köster A, Muñoz-Muñoz YM, Vrabec J. Molecular modeling and
805   simulation: Force field development, evaporation processes and thermophysical properties of
806   mixtures. High Performance Computing in Science and Engineering '18. 2019, p. 457-74.
807   https://doi.org/10.1007/978-3-030-13325-2_29.

808 [49] Walther J H, Koumoutsakos P. Molecular dynamics simulation of nanodroplet evaporation. Journal
809   of Heat Transfer 2001, 23: 741-8. https://doi.org/10.1115/1.1370517.

810   [50] Vrabec J, Kedia GK, Fuchs G, Hasse H. Comprehensive study of the vapour–liquid coexistence of

811   the truncated and shifted Lennard–Jones fluid including planar and spherical interface properties.

812   Molecular Physics 2006; 104(9): 1509-27. https://doi.org/10.1080/00268970600556774.

813   [51] Rana AS, Lockerby DA, Sprittles JE. Lifetime of a nanodroplet: Kinetic effects and regime transitions.

814   Physical Review Letters 2019; 123. https://doi.org/10.1103/PhysRevLett.123.154501.

815   [52] Thompson SM, Gubbins KE, Walton JPRB, Chantry RAR, Rowlinson JS. A molecular dynamics

816   study of liquid drops. The Journal of Chemical Physics 1984; 81(1): 530-42.

817   https://doi.org/10.1063/1.447358.

818   [53] van Giessen A E, Blokhuis E M. Determination of curvature corrections to the surface tension of a

819   liquid–vapor interface through molecular dynamics simulations. The Journal of Chemical Physics

820   2002; 116. https://doi.org/10.1063/1.1423617.

821   [54] Langroudi SMM, Ghassemi M, Shahabi A, Nejad HR. A molecular dynamics study of effective

822   parameters on nano-droplet surface tension. Journal of Molecular Liquids 2011; 161: 85-90.

823   https://doi.org/10.1016/j.molliq.2011.04.011.

824   [55] Sumardiono S, Fischer J. Molecular simulations of droplet evaporation by heat transfer. Microfluid

825   Nanofluid 2007; 3: 127-40. https://doi.org/10.1007/s10404-006-0110-y.

826   [56] Long L N, Micci M M, Wong B C. Molecular dynamics simulations of droplet evaporation. Computer

827   Physics Communications 1996; 96: 167-72.

828   [57] Consolini L, Aggarwal S K, Murad S. A molecular dynamics simulation of droplet evaporation.

829   International Journal of Heat and Mass Transfer 2003; 46: 3179–88.

830   https://doi.org/10.1016/S00179310(03)00101-7.

831   [58] Kaltz T L, Long L N, Micci M M, Little J K. Supercritical vaporization of liquid oxygen droplets

832   using molecular dynamics. Combustion Science and Technology 1998; 136: 279-301.

833   https://doi.org/10.1080/00102209808924174.

834   [59] Zhang Y, Jia M, Yi P, Chang Y, He Z, Wang Q. A molecular dynamics study of binary-component

835   n-alkane fuel vaporization characteristics at sub/supercritical nitrogen environments. Proceedings of

836   the Combustion Institute 2020. https://doi.org/10.1016/j.proci.2020.06.108.

837   [60] Manin J, Crua C, Pickett LM. Transcritical mixing of sprays for multi-component fuel mixtures.

838   Proceedings ILASS–Europe 2017. 28th Conference on Liquid Atomization and Spray Systems. 2017.

839   http://dx.doi.org/10.4995/ILASS2017.2017.5065.

840   [61] Kitano T, Nishio J, Kurose R, Komori S. Evaporation and combustion of multicomponent fuel

841   droplets. Fuel 2014; 136: 219-25. http://dx.doi.org/10.1016/j.fuel.2014.07.045.

[62] Poulton L, Rybdylova O, Zubrilin IA, Matveev SG, Gurakov NI, Al Qubeissi M, et al. Modelling of multi-component kerosene and surrogate fuel droplet heating and evaporation characteristics: A comparative analysis. Fuel 2020; 269. https://doi.org/10.1016/j.fuel.2020.117115.

[63] Raghavan V. Numerical modeling of evaporation and combustion of isolated liquid fuel droplets: A review. Journal of the Indian Institute of Science 2019. https://doi.org/10.1007/s41745-019-0097-5.

[64] Miyagawa H, Nagaoka M, Ohsawa K, Yamada T. Spray vaporization model for multi-component gasoline. JSAE Review 1998; 19: 299–304.

[65] Myong K-J, Suzuki H, Senda J, Fujimoto H. Spray inner structure of evaporating multi-component fuel. Fuel 2008; 87: 202-10. https://doi.org/10.1016/j.fuel.2007.04.017.

[66] Manin J, Pickett L M, Crua C. Microscopic observation of miscible mixing in sprays at elevated temperatures and pressures. ILASS Americas 27th Annual Conference on Liquid Atomization and Spray Systems. Raleigh, NC; 2015.

[67] Banuti DT. Crossing the Widom-line – Supercritical pseudo-boiling. The Journal of Supercritical Fluids 2015; 98: 12-6. http://dx.doi.org/10.1016/j.supflu.2014.12.019.

[68] Xu L, Kumar P, Buldyrev S V, Chen S H, Poole P H, Sciortino F, Stanley H E. Relation between the Widom line and the dynamic crossover in systems with a liquid–liquid phase transition. Proceedings of the National Academy of Sciences of the United States of America 2005; 102:16558-62. www.pnas.org/cgi/doi/10.1073/pnas.0507870102.

[69] Maxim F, Contescu C, Boillat P, Niceno B, Karalis K, Testino A, et al. Visualization of supercritical water pseudo-boiling at Widom line crossover. Nature Communications 2019. https://doi.org/10.1038/s41467-019-12117-5.

[70] Yoon T J, Ha M Y, Lee W B, Lee Y-W. Monte Carlo simulations on the local density inhomogeneities of sub- and supercritical carbon dioxide: Statistical analysis based on the Voronoi tessellation. The Journal of Supercritical Fluids 2017; 119: 36-43. http://dx.doi.org/10.1016/j.supflu.2016.09.001.

[71] Plimpton S. Fast Parallel Algotithms for Short-Range Molecular Dynamics. Journal of Computational Physics 1995; 117: 1–19.

[72] Cao B-Y, Xie J-F, Sazhin S S. Molecular dynamics study on evaporation and condensation of n-dodecane at liquid-vapor phase equilibria. The Journal of Chemical Physics 2011; 134. https://doi.org/10.1063/1.3579457.

[73] Martin M G, Siepmann J I. Transferable Potentials for Phase Equilibria. 1. United-Atom Description of n-Alkanes. The Journal of Physical Chemistry B 1998; 102. https://doi.org/10.1021/jp972543.

873 [74]Martin M G, Siepmann J I. Novel Configurational-Bias Monte Carlo Method for Branched Molecules.

874 Transferable Potentials for Phase Equilibria. 2. United-Atom Description of Branched Alkanes. The

875 Journal of Physical Chemistry B 1999; 103(21): 4508-17. https://doi.org/10.1021/jp984742e.

876 [75] Wick C D, Martin M G, Siepmann J I. Transferable Potentials for Phase Equilibria. 4. United-Atom

877 Description of Linear and Branched Alkenes and Alkylbenzenes. The Journal of Physical Chemistry

878 B 2000; 104. https://doi.org/10.1021/jp001044x.

879 [76] Allen M P, Tildesley D J. Computer Simulation of Liquids. 2nd ed.; 2017.

880 [77] Nath S K, Escobedo F A, de Pablo J J. On the simulation of vapor–liquid equilibria for alkanes. The

881 Journal of Chemical Physics 1998; 108: 9905-11.

882 [78] Jorgensen W L, Madura J D, Swenson C J. Optimized Intermolecular Potential Functions for Liquid

883 Hydrocarbons. Journal of the American Chemical Society 1984; 106: 6638-46.

884 [79] Andersen H C. Rattle: A "velocity" version of the shake algorithm for molecular dynamics

885 calculations. Journal of Computational Physics 1983; 52: 24–34.

886 [80] Lin H-M, Kim H, Chao K-C. Gas-liquid Equilibria in Nitrogen + n-Hexadecane Mixtures at Elevated

887 Temperatures and Pressures. Fluid Phase Equilibria 1981; 7: 181-5.

888 [81] Avlonitis G, Mourikas G, Stamataki S, Tassios D. A generalized correlation for the interaction

889 coefficients of nitrogen- hydrocarbon binary mixtures. Fluid Phase Equilibria 1994; 101: 53-68.

890 [82] García-Sánchez F, Eliosa-Jiménez G, Silva-Oliver G, Godínez-Silva A. High-pressure (vapor+liquid)

891 equilibria in the (nitrogen+n-heptane) system. The Journal of Chemical Thermodynamics 2007; 39:

892 893-905. https://doi.org/10.1016/j.jct.2006.11.007.

893 [83] Qiu L, Reitz R D. Condensation processes in a motoring engine. The Journal of Supercritical Fluids

894 2014; 90: 84-100. http://dx.doi.org/10.1016/j.supflu.2014.03.013.

895 [84] Qiu L, Reitz R D . An investigation of thermodynamic states during high-pressure fuel injection using

896 equilibrium thermodynamics. International Journal of Multiphase Flow 2015; 72: 24-38.

897 http://dx.doi.org/10.1016/j.ijmultiphaseflow.2015.01.011.

898 [85] Peng D-Y, Robinson D B. A new two-constant equation of state. Industrial Engineering Chemistry

899 Research Fundamentals 1976; 15: 59-64.

900 [86] Poling B E, Prausnitz J M, O'Connell J P. The Properties of Gases and Liquids. 5th ed.; 2004.

901 [87] García-Sánchez F, Eliosa-Jiménez G, Silva-Oliver G, Vázquez-Román R. Vapor–liquid equilibria of

902 nitrogen–hydrocarbon systems using the PC-SAFT equation of state. Fluid Phase Equilibria 2004;

903 217: 241-53. https://doi.org/10.1016/j.fluid.2003.05.002.

[88] Li C C. Critical temperature estimation for simple mixture. The Canadian Journal of Chemical Engineering 1971; 49: 709–10.

[89] Kreglewski A, Kay W B. The critical constants of conformal mixtures. The Journal of Physical Chemistry 1969; 73: 3359– 66.

[90] Tuckerman M E, Martyna G J. Understanding modern molecular dynamics: Techniques and applications. The Journal of Physical Chemistry B 2000; 104: 159-78. https://doi.org/10.1021/jp992433y.

[91] Ghassemi H, Baek S W, Khan Q S. Experimental Study on Binary Droplet Evaporation at Elevated Pressures and Temperatures. Combustion Science and Technology 2006; 178: 1031-53. https://doi.org/10.1080/00102200500296697.

[92] Ghassemi H, Baek S W, Khan Q S. Experimental Study on Binary Droplet Evaporation at Elevated Pressure and Temperature. 43rd AIAA Aerospace Sciences Meeting and Exhibit. 2005. https://doi.org/10.2514/6.2005-353.

[93] Rycroft C H. VORO++: A three-dimensional voronoi cell library in C++. Chaos 2009; 19. https://doi.org/10.1063/1.3215722.

[94] Fern J T, Keffer D J, Steele W V. Vapor-liquid equilibrium of ethanol by molecular dynamics simulation and Voronoi tessellation. The Journal of Physical Chemistry B 2007; 111: 13278-86. https://doi.org 10.1021/jp075414u.

[95] Morin C, Chauveau C, Dagaut P, GÖKalp I, Cathonnet M. Vaporization and oxidation of liquid fuel droplets at high temperature and high pressure: Application to n-alkanes and vegetable oil methyl esters. Combustion Science and Technology 2004; 176: 499-529. http://dx.doi.org/10.1080/00102200490276719.

[96] Sato J. Studies on droplet evaporation and combustion in high pressures. 31st Aerospace Sciences Meeting. 1993.

[97] Zhu G S, Aggarwal S K. Transient supercritical droplet evaporation with emphasis on the effects of equation of state. International Journal of Heat and Mass Transfer 2000; 43: 1157-71.

[98] Wu HL, Nie WS, Zheng Z, Liu Y. Migration and Evaporation Characteristics of Kerosene Droplet in Supercritical Environment. MATEC Web of Conferences 2019; 257. https://doi.org/10.1051/matecconf/201925701002.

[99] Banuti DT, Raju M, Ihme M. Between supercritical liquids and gases – reconciling dynamic and thermodynamic state transitions. The Journal of Supercritical Fluids 2020; 165. https://doi.org/10.1016/j.supflu.2020.104895.

936 [100] Raju M, Banuti DT, Ma PC, Ihme M. Widom lines in binary mixtures of supercritical fluids.
937   Scientific Reports 2017; 7. https://doi.org/10.1038/s41598-017-03334-3.

938 [101] Konynenburg P H V, Scott R L. Critical lines and phase equilibria in binary Van der waals mixtures.
939   Philosophical Transactions of the Royal Society A: Mathematical, Physical and Engineering Sciences
940   1980; 298. https://doi.org/10.1098/rsta.1980.0266.

941 [102] Han K, Song G Q, Ma X K, Yang B. An experimental and theoretical study of the effect of
942   suspended thermocouple on the single droplet evaporation. Applied Thermal Engineering 2016; 101:
943   568–75. http://dx.doi.org/10.1016/j.applthermaleng.2015.12.022.

944 [103] Wang J G, Wang X R, Ren G L, Xiang K. Effect of ambient condition on n-heptane droplet
945   evaporation. Mathematical Modelling of Engineering Problems 2017; 4: 13-7.
946   https://doi.org/10.18280/mmep.040103.

947

948

949

950